Atomic Structures and Doping Effects in Intercalated Few-layer Graphene

By

Jason P. Bonacum

Dissertation
Submitted to the Faculty of the
Graduate School of Vanderbilt University
in partial fulfillment of the requirements
for the degree of

DOCTOR OF PHILOSOPHY
in
Physics

May 31, 2020
Nashville, Tennessee

Approved by:

Dr. Richard F. Haglund

Dr. Kirill I. Bolotin

Dr. Sokrates T. Pantelides

Dr. Janet E. Macdonald

ACKNOWLEDGEMENTS

The person I am today, at the end of my journey as a graduate student, has been shaped by many people in my life. First, I thank my advisors, Richard Haglund, Kirill Bolotin, and Sokrates Pantelides. Their patience and guidance had an essential role in this work and my growth as a scientist. They taught me how to form scientific questions with precise hypotheses, to develop realist methods for testing my hypotheses, and how to clearly communicate the results. More importantly though, their encouragement pushed me to figure out solutions to problems and create my own original ideas. I am fortunate to have them as colleagues, and I hope to continue working with them throughout our scientific endeavors. Also, thank you, Janet Macdonald and Clare McCabe, for being on my PhD committee. The breadth of knowledge you both bring to this work ensures that I become a well-rounded scientist, and I very much appreciate your comments and suggestions.

A special thanks also goes to all of my excellent colleagues who directly contributed to this work. Thank you, Andy O’Hara, Oleg Ovchinnikov, De-Liang, and Yan-Fang Zhang, for doing the essential theoretical and computational work used in this dissertation. I would not have been able to include the density-functional-theory calculations, image simulations, and principal component analysis without your expertise and dedication. I am also particularly grateful for Andy’s patience with answering my persistent questions and helping me interpret data. Thank you, Georgy Gordeev, Sonakshi Arora, and Stephanie Reich, for doing the resonance-Raman spectroscopy used in this dissertation, which was a crucial for determining the doping effects of intercalants and expanding the scope of this work. I also want to thank Juan-Carlos Idrobo for his

commitment to my work at Oak Ridge National Laboratory (ORNL). Thank you for all the long hours you put in on the microscope and helping me get data for this work while I was on a tight schedule.

Additionally, thank you to all the lab mates and staff members that have helped me throughout my research at Vanderbilt University. Andrey Klots, Dhiraj Prasai, and Ryan Nicholl helped teach me various fabrication, measurement, and theory techniques during my first years in graduate school, and they were crucial to my early development as a graduate student. Thank you to my classmates, Austin Howes and Ben Weintrub, for the many fruitful discussions about our research during lunch and the grinding late-nights in the lab. Thank you Tony Hmelo, Kurt Heinrich, Alice Leach, Bill Martinez, and Dmitry Koktysh, the staff members of the Vanderbilt Institute of Nanoscale Science and Engineering (VINSE), for taking the time to train me on instruments, assist me with process development, and help me with problems in the VINSE facilities.

Finally, I am especially grateful for all the support my friends and family have given me during tough times. I could not have made it to this point without their love and encouragement. My parents have always pushed me to do what I believe is important in the world, and I consider this work to be a valuable part of my contribution so far. A special thanks also goes to my girlfriend, Jessica, for being there to get my mind off work when I need it and helping me proof-read the things I write after staying up too late. All of you will forever have my gratitude!

TABLE OF CONTENTS

Page

Chapter

LIST OF TABLES

LIST OF FIGURES

LIST OF ABBREVIATIONS

ADF	Annular Dark-Field
AFM	Atomic Force Microscopy
AZO	Aluminum-doped Zinc Oxide
BCS	Bardeen-Cooper-Schrieffer
BEMA	Bisphenol A Ethoxylate Dimethacrylate
BLG	Bilayer Graphene
CVT	Chemical Vapor Transport
DFT	Density Functional Theory
DOS	Density of States
EBL	Electron Beam Lithography
EDL	Electric Double Layer
EELS	Electron Energy Loss Spectroscopy
FFT	Fast Fourier Transform
FLG	Few-Layer Graphene
GIC	Graphite Intercalation Compound
IPA	Isopropyl Alcohol
ITO	Indium Tin Oxide
MIBK	Methyl Isobutyl Ketone
MW	Molecular Weight
PCA	Principal Component Analysis
PDMS	Polydimethylsiloxane

PEGMA	Poly(Ethylene Glycol) Methyl Methacrylate
PEO	Polyethylene Oxide
PID	Proportional-Integral-Derivative
PMMA	Polymethyl Methacrylate
STEM	Scanning Transmission Electron Microscopy
TFSI	Bis(Trifluoromethanesulfonyl)imide ion
UV	Ultraviolet
VINSE	Vanderbilt Institute of Nanoscale Science and Engineering
XRD	X-Ray Diffraction

LIST OF PUBLICATIONS

Portions of this dissertation have been drawn from the following publication:

Bonacum, J. P., O’Hara, A., Bao, D., Ovchinnikov, O. S., Zhang, Y., Gordeev, G., Arora, S., Reich, S., Idrobo, J., Haglund, R. F., Pantelides, S. T., & Bolotin, K. I. (2019). Atomic-resolution visualization and doping effects of complex structures in intercalated bilayer graphene. *Physical Review Materials*, **3**, 064004.

CHAPTER 1

Introduction

1.1 Introduction to Intercalation Compounds

Graphite intercalation compounds (GICs), layers of atoms or molecules inserted in between the layers of carbon, have been studied for over a century for potential applications in energy storage, superconductivity, and reaction catalysis (Dresselhaus & Dresselhaus, 2002; Nitta, Wu, Lee, & Yushin, 2015; Shimizu & Kamimura, 1983). The relatively low strength of van der Waals forces that bind together the crystalline carbon layers together allows for repeatable insertion and diffusion of a wide variety of atomic species in the interlayer gap. Alkali metals are common intercalants for graphite that have an important role in lithium-ion battery technology, which utilizes intercalation of lithium ions as the mechanism to store charge. Other common intercalants for GICs are polyatomic ions, *e.g.* hexafluorophosphate and bistriflimide, which have possible applications in dual-graphite batteries (Beltrop, Beuker, Heckmann, Winter, & Placke, 2017; Fan, Qi, & Wang, 2017; Read, Cresce, Ervin, & Xu, 2014; Rothermel et al., 2014).

1.1.1 Applications of Graphite Intercalation Compounds

Collecting data about the atomic structure and doping effects (*i.e.* raising/lowering of the Fermi level in the carbon layers) of intercalants in GICs is essential to understanding the mechanisms of superconductivity, reaction catalysis, energy storage, and other phenomena and applications related to GICs. For example, superconductivity in alkali metal GICs was first explored because of the high Debye frequency in graphite and the high doping levels achieved by intercalation, which are necessary for Bardeen-Cooper-Schrieffer (BCS) superconductivity (Bardeen, Cooper, & Schrieffer, 1957). Graphite intercalated with sodium, potassium, rubidium, cesium, calcium, and ytterbium have all exhibited superconductivity with critical temperatures of 5 K, 0.55 K, 0.15 K, 0.135 K, 11.5 K, and 6.5 K, respectively (Al-Jishi, 1983; Csányi, Littlewood, Nevidomskyy, Pickard, & Simons, 2005; Weller, Ellerb, Saxena, Smith, & Skipper, 2005). The wide range of critical temperatures suggests that the emergence of superconductivity is not caused purely by the doping of carbon layers in the graphite because all the intercalants listed above provide similar amounts of doping, measured by the shift of the Fermi level in the carbon layers. Superconductivity in these GICs is in fact partly due to structural ordering of intercalants in the van der Waals gaps and formation of interlayer states from the intercalant s-bands (Al-Jishi, 1983; Csányi et al., 2005).

Alkali metal GICs have also been extensively studied for applications in redox reactions and catalysis. These GICs maintain the reducing capabilities of the alkali metals while forming an anisotropic laminar structure that has proved to be useful for stereoselective reactions (Boersma, 1974; Lalancette, Rollin, & Dumas, 1972; Rakoczy, Klimkiewicz, & Morawski, 1996). Additionally, delocalization of the alkali metal valence electron into the π-bands of the graphite (*i.e.* doping of the carbon layers by the alkali metal intercalants) makes alkali metal GICs useful as catalysts in polymerization reactions (Boersma, 1974; Lalancette et al., 1972; Podall & Foster, 1958).

The most common application of GICs is for energy storage. Lithium-ion batteries use intercalation compounds as electrodes to store charge in the form of lithium ions. The lithium ions leave the cathode and intercalate into the anode when charging. The process reverses during the discharge of the battery when the lithium ions deintercalate from the anode and intercalate into the cathode. Common commercially available cathode materials include lithium cobalt oxide and lithium iron phosphate, but graphite (recently combined with silicon particles) is the anode material in all currently mass-produced lithium-ion batteries (Nitta et al., 2015; Tarascon & Armand, 2001; Yoshino, 2012). Although the atomic structure of lithium GICs is well understood, novel intercalation electrodes are being developed with graphite in which the atomic structures of the intercalants are not fully understood (Dresselhaus & Dresselhaus, 2002; Ebert, 1984; Nitta et al., 2015; Tarascon & Armand, 2001; Z. hong Yang & Wu, 2001). Some of the chemistries used for these novel battery electrodes include cointercalation of solvent molecules with alkali metal ions and intercalation of polyatomic ions in dual-graphite electrode batteries (Azhagurajan, Kajita, Itoh, Kim, & Itaya, 2016; Beltrop et al., 2017; Cohn, Muralidharan, Carter, Share, & Pint, 2016; Fan, Qi, & Wang, 2017; Rothermel et al., 2014; Wen et al., 2014; Yabuuchi, Kubota, Dahbi, & Komaba, 2014). The polyatomic intercalants in these types of electrodes can exist in multiple locations, orientations, and conformations inside graphite. These atomic structures are more complex and difficult to identify compared to spherically symmetric intercalants such as lithium, where only the positions of the lithium ions are relevant to the atomic structure, but understanding the orientation and conformation of polyatomic intercalants is crucial for developing these intercalation compounds for energy storage applications.

The orientation and conformation of polyatomic intercalants affect the interlayer spacing of the carbon layers and the intralayer spacing of the intercalants, which determines the expansion of graphite electrodes during charging/discharging and the charge capacity of the electrodes (Tasaki, 2014). Additionally, interactions between intercalants may cause bonds to form, changing the final electrochemical potential of the intercalation products and thus the nominal voltage of the electrodes in battery applications. All these factors illustrate why detailed measurements of atomic structures in intercalation products are a key to developing novel intercalation electrode materials.

1.1.2 Few-layer Graphene Intercalation Compounds

Most of the research on intercalation has been done with bulk graphite. However, the recent isolation of graphite with controlled number of carbon layers has led to a surge of interest in intercalated few-layer graphene (FLG) and bilayer graphene (BLG). These few-layer intercalation compounds have distinctly different properties compared to bulk GICs (Hui, Burgess, Zhang, & Rodríguez-López, 2016; Wan et al., 2016). For example, BLG intercalated with lithium exhibits faster diffusion and greater density of lithium atoms than graphite intercalated with lithium (Kühne et al., 2018, 2017). In general, FLG in the form of composites and foams is an attractive material for innovative intercalation battery electrodes due to fast intercalant diffusion, mechanical flexibility, high electrical and thermal conductivity, and the ability to accept a variety of intercalant species (Cohn, Share, Carter, Oakes, & Pint, 2016; Palumbo et al., 2019; Qi et al., 2015; Share, Cohn, Carter, & Pint, 2016; Zhang, Chen, Luo, Zhou, & Liu, 2017).

Intercalated FLG also maintains some of the properties of monolayer graphene, such as high transparency, high electron mobility, and mechanical flexibility (Bao et al., 2014; Khrapach et al., 2012; Wan et al., 2016; W. Zhao, Tan, Liu, & Ferrari, 2011). Graphene is a semimetal with a high carrier mobility greater than 1000 $cm^2V^{-1}s^{-1}$ and 80% visible transparency when placed on SiO_2 (K. S. Kim et al., 2009). Other research groups have also reported carrier mobilities as high as 4×10^4 $cm^2V^{-1}s^{-1}$ and visible transparencies as high as 95% (J.-H. Chen, Jang, Xiao, Ishigami, & Fuhrer, 2008; Woltornist, Oyer, Carrillo, Dobrynin, & Adamson, 2013). This high mobility gives graphene the potential to achieve higher conductivity than conductive metal oxides and metallic thin films, but the conductivity of pristine graphene is limited by the low carrier density (Gusynin, Sharapov, & Carbotte, 2006; X. Huang et al., 2016; Pierantoni et al., 2015). However, the carrier density in graphene can be increased with a variety of doping methods. Electrostatic doping with ionic liquids and polymer electrolytes achieves carrier densities on the order of 10^{14} cm^{-2}, but this method requires a constant voltage supply to maintain the carrier density (F. Chen, Qing, Xia, Li, & Tao, 2009; Froehlicher & Berciaud, 2015). Chemical doping *via* nitrogen or boron substitution achieves similar carrier densities without an applied voltage, but this method significantly lowers the carrier mobility due to scattering from defects around the substitution sites (Joucken, Henrard, & Lagoute, 2019; S. J. Kim et al., 2016; H. Liu, Liu, & Zhu, 2011; Lv et al., 2012; Wei et al., 2009).

Fortunately, large doping levels on the order of 10^{15} cm^{-2} can be achieved with intercalation, and intercalants do not disrupt the intralayer chemical bonds in the graphene layers (Wan et al., 2016; W. Zhao et al., 2011). Recent work has demonstrated that intercalated FLG maintains high optical transparency while providing high conductivity greater than that of indium tin oxide (ITO), aluminum-doped zinc oxide (AZO), carbon nanotubes, and chemically doped graphene (Bao et al., 2014; Khrapach et al., 2012). These characteristics make few-layer GICs an attractive platform for studying superconductivity and plasmons in highly doped graphene and for applications as flexible transparent conductors, thermal diffusers, radio frequency attenuators, and electrocatalysts (Bezares et al., 2017; Bointon et al., 2015; Kanetani et al., 2012; Khrapach et al., 2012; Lu & Zhao, 2013; Pierantoni et al., 2015; Shirodkar et al., 2018; Wan et al., 2016).

1.2 Present Work

This dissertation addresses the questions of whether intercalated molecules interact to form ordered structures and how these structures affect the electronic properties of the host material, *i.e.* FLG. We hypothesize that polyatomic intercalants form various crystalline monolayers, which differ in composition depending on the reaction conditions, and that these distinct crystalline structures have different doping effects in the adjacent graphene layers. The atomic structures formed in GICs and few-layer GICs have been commonly characterized by spatially averaged techniques such as x-ray diffraction (XRD) and Raman spectroscopy (Asher, 1959; Axdal & Chung, 1987; Cohn, Share, et al., 2016; Dimiev et al., 2013; Rothermel et al., 2014; W. Zhao et al., 2011). In the present work, we use aberration-corrected scanning transmission electron microscopy (STEM) to atomically resolve the structures formed by molecules intercalated in FLG and BLG.

Device architectures that implement electrochemical intercalation for *in situ* STEM and chemical vapor transport (CVT) intercalation methods for *ex situ* STEM are described in detail (chapter 2). By using intercalated BLG, we image a single layer of intercalants to observe how the molecules interact and bond with each other in the van der Waals gap. For intercalated FLG, we combine the STEM images with STEM simulations and examine the orientation of intercalants between layers. We combine the STEM images with electron energy loss spectroscopy (EELS) in real time to unambiguously determine chemical composition and oxidation state of the intercalants. Aberration-corrected STEM combined with EELS also allows us to directly visualize and characterize local atomic structures such as defects and phase boundaries in the intercalant layers. Additionally, we use optical measurements such as Raman spectroscopy to investigate the effects of the observed intercalated structures on the electronic properties of the surrounding graphene layers. The data in this dissertation are crucial for interpreting Raman spectra of intercalated FLG, which depend on the atomic and electronic structure of the material, and demonstrates that intercalation of molecules can be used to create novel monolayer materials.

CHAPTER 2

Intercalation Methods and Experimental Techniques

2.1 Electrochemical Intercalation

Although the intercalation dynamics of FLG and bulk graphite are different, the intercalation process is executed in similar ways. Electrochemical intercalation is a common method to control the intercalation process in real time. The intercalants are dissolved in an electrolyte that covers the FLG sample and intercalation is induced by applying a voltage bias between the FLG and a counter electrode inside the electrolyte.

2.1.1 Intercalation Devices for Few-Layer Graphene

The intercalation devices are similar to field effect transistors where the FLG acts as the gate channel and the electrolyte acts as the gate dielectric. An optical image of this type of device is shown in figure 2.1a. The electrodes are defined lithographically, and the electrolyte is drop-cast over the electrodes. The source and drain are metal contacts on the FLG, and the gate electrode is another metal electrode in the electrolyte that does not contact the FLG. The fabrication protocols for these types of devices are given in appendix A.

When a bias is applied between the FLG and the gate electrode, ions of opposite charge migrate to the surface of the FLG and gate electrode forming a charged layer above the respective electrodes. For example, if a positive voltage is applied to the gate electrode in an electrolyte composed of positive lithium ions and negative bis(trifluoromethanesulfonyl)imide ions (TFSI), then the positive lithium ions will migrate to the surface of the FLG as shown in figure 2.1b. This layer of positively charged lithium ions causes electrons to be drawn into the

FLG from the source electrode resulting in more free carriers and thus higher conductivity in the FLG. Most of the electrical potential drop across the device occurs at this interface between the ion layer and the electrode surface as illustrated in figure 2.1b, which act like plates of a capacitor storing charge when a voltage bias is applied. These two charged layers are known as the electric double layer (EDL). By also applying a bias between the source and drain electrodes, the change in conductivity can be observed as a change in the source-drain current as plotted in figure 2.2c for a monolayer graphene device.

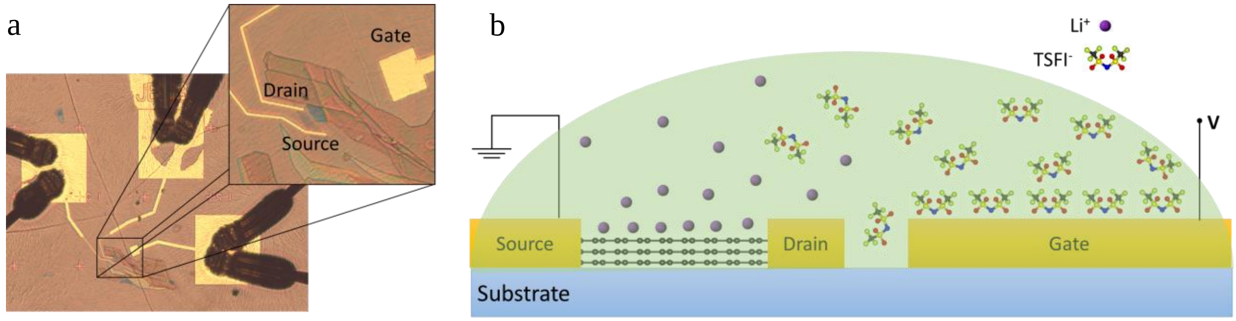

Figure 2.1: (a) Optical image of an electrolytic field effect transistor with FLG as the gate channel (b) A diagram of the device viewed from the side displaying migration of the different ions under positive gate bias.

The ions can intercalate between the layers of graphene as well as migrate to the outer surface. This migration of ions occurs at any finite voltage. The rate of migration is governed by the ion conductivity of the solvent, and the charge density in the EDL is governed by the effective size of the ions and solvation shell (*i.e.* the shell of polarized solvent molecules that encapsulates the ions). However, intercalation of the ions only occurs at voltage biases for which the electrochemical potential of the ions in solution is higher than that of ions intercalated in the FLG. The voltage at which intercalation occurs and the number of intercalants that enter the material are conventionally measured with electrochemical techniques such as voltammetry and coulometry, but these techniques are difficult to implement on single flakes of FLG.

The first reason why electrochemical measurement techniques are difficult to implement is that devices made with a single flake of FLG are challenging to fabricate with a standard reference electrode. The gate electrode discussed previously is acting as the counter electrode to apply the bias and measure the current through the device, and this electrode is made of metals such as gold, platinum, or titanium that can be easily deposited using evaporative techniques. We make the counter electrode much larger than the FLG flake (see figure 2.1a) to establish an electrochemical potential by EDL formation rather than by a faradaic process (the reduction or oxidation of a chemical substance at the electrode surface). This device architecture allows us to apply a bias and measure the current to the FLG (the working electrode), but we cannot measure the potential drop with respect to a standard faradaic process. Ideally, we would fabricate an additional reference electrode made of lithium for the example device given in figure 2.1. A lithium electrode will release or consume (oxidize or reduce) lithium atoms in the electrolyte during the reaction and maintain a constant electrochemical potential with respect to the electrolyte, but fabricating a lithographically defined lithium electrode is difficult due to the high reactivity of lithium metal. Lithium will react with air and even pure nitrogen gas, requiring all the fabrication steps to be performed in an argon environment.

The second reason why electrochemical measurement techniques are difficult to implement on single flakes of FLG has to do with the microscopic size of the flakes. The FLG flakes achieved by mechanical exfoliation are only on order of 10 μm in size and can only hold a small amount of lithium. For example, a 10 μm by 10 μm square of BLG can only hold $5.5x10^8$ lithium atoms, corresponding to 89 pC of charge, and a flake of this size can take as long as a minute to fully intercalate. This rate of intercalation only produces a few picoamperes of current, which is many orders of magnitude smaller than the microamperes of ionic current in the electrolyte.

These two restrictions make it difficult to determine when and how many intercalants enter the FLG by electrochemical measurement techniques. We can only measure the current through the device without a reference electrode, but the current is dominated by the ionic current instead of the faradaic current from intercalation. Because of these restrictions, we use Raman spectroscopy to monitor the intercalation process by examining changes the spectra of the graphene layers as a function of applied voltage.

2.1.2 Raman Spectroscopy of Doped Graphene

Intercalation causes a change in the number of the free carriers, often referred to as doping, inside the graphene layers that hold the intercalants. Therefore, it is crucial to know how the Raman spectra of graphene change as the amount of doping changes. Raman spectroscopy probes vibrational modes of a material (*i.e.* phonons) by scattering monochromatic photons. The photons interact with the phonons in the graphene lattice and scatter inelastically, resulting in a shift of the photon energy by the energy of the phonon known as the Raman shift. When dopants are introduced to a material, the additional free carriers electronically screen the lattice and typically cause softening of the phonon modes, thus reducing (red shifting) the Raman shift of the spectral peak for that phonon mode.

We focus on the G mode Raman peak, or G peak, to examine the doping effects in the graphene layers. The G peak blue shifts with doping due to the Kohn anomaly in the phonon band structure of graphene (Das et al., 2008; Froehlicher & Berciaud, 2015; Lazzeri & Mauri, 2006). A Kohn anomaly is an anomalous lowering of the phonon energy at high symmetry points in the first Brillouin zone. Several parts of the Fermi surface are connected by wave vectors of specific phonon modes at these symmetry points, and an abrupt increase in the screening of the lattice occurs when the phonon wave vector equals twice the wave vector of the electrons at the Fermi surface. The Kohn anomaly in graphene occurs for the G mode at the high-symmetry K point, but as dopants increase the Fermi level in graphene, the wave vector of the electrons at the Fermi surface increases and breaks the conditions required for the Kohn anomaly (Lazzeri & Mauri, 2006; Malard, Pimenta, Dresselhaus, & Dresselhaus, 2009). Therefore, the screening of the lattice decreases, stiffening the phonons and increasing (blue shifting) the Raman shift of the G peak.

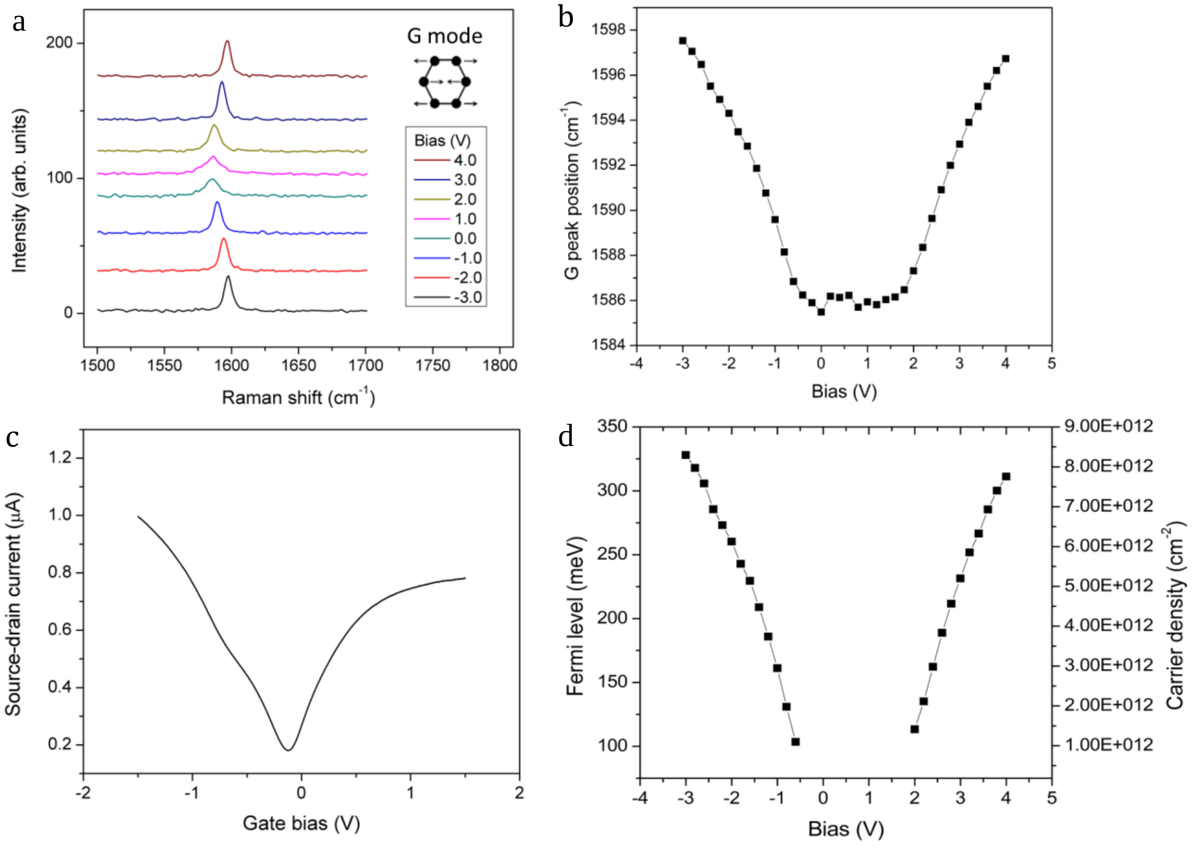

Figure 2.2: (a) G mode Raman peak of monolayer graphene at different gate biases for an electrolyte field effect transistor device (b) A plot the G peak position vs gate bias for the same device (c) Source-drain current in graphene as a function of gate bias applied to the electrolyte (d) A plot of Fermi level and carrier density vs gate bias, calculated using the phenomenological method in (Froehlicher & Berciaud, 2015).

This shifting of the G peak is displayed in figure 2.2a & 2.2b for a monolayer graphene device using the same architecture as figure 2.1. The Fermi energy of the electrons at the Fermi surface in graphene, plotted in figure 2.2d, is calculated using a linear phenomenological fit (Froehlicher & Berciaud, 2015). However, this calculation only gives an estimate of the Fermi energy because the trend of the G peak position vs Fermi energy becomes sublinear at higher doping levels. For more precise calculations of the Fermi energy at the high doping levels that occur during intercalation, we use the more sophisticated resonance-Raman technique that is discussed in chapter 5. The carrier density (n) for the graphene device is also calculated and plotted in figure 2.2d. This calculation is accomplished using the Fermi energy (E_F) and density of state (D(E)) near the K point in graphene, BLG, or FLG, depending on the number of graphene layers that are used in the device. These equations are displayed in table 1 (Castro Neto, Guinea, Peres, Novoselov, & Geim, 2009; Dresselhaus & Dresselhaus, 2002; Nilsson, Neto, Guinea, & Peres, 2006; Wallace, 1947).

	General equation	Monolayer graphene	Bilayer graphene	Few-layer graphene
Density of states	$\mathrm{D(E)} = \frac{1}{\mathrm{A}}\frac{\mathrm{dN}}{\mathrm{dE}}$	$\frac{2}{\pi}\frac{\mathrm{E}}{(\mathrm{v_F}\hbar)^2}$	$\frac{2}{\pi}\frac{\gamma}{(\mathrm{v_F}\hbar)^2}$	$\frac{2}{\pi}\frac{\mathrm{m}^*}{\hbar^2}$
Carrier density	$\mathrm{n} \cong \int_0^{\mathrm{E_F}} \mathrm{D(E)dE}$	$\frac{2}{\pi}\frac{\mathrm{E_F}^2}{(\mathrm{v_F}\hbar)^2}$	$\frac{2}{\pi}\frac{\gamma \mathrm{E_F}}{(\mathrm{v_F}\hbar)^2}$	$\frac{2}{\pi}\frac{\mathrm{m}^*\mathrm{E_F}}{\hbar^2}$

Table 2.1: Equations for the density of states and carrier density in monolayer, bilayer, and few-layer graphene. The density of states is expressed per unit energy and unit area. The carrier density is calculated by integrating the density of states up to the Fermi energy in energy space. We approximate the Fermi-Dirac distribution as a step function so that no states are occupied above the Fermi energy, which is a reasonable approximation at room temperature.

Numeric values for the variables are given below.

Fermi velocity:	$\mathrm{v_F} = 10^6\ \mathrm{m/s}$
Interlayer coupling energy:	$\gamma = 400\ \mathrm{meV}$
Electron effective mass:	$\mathrm{m}^* = 0.067\mathrm{m_0} = 6.10 \times 10^{-32}\ \mathrm{kg}$

2.1.3 Signatures of Intercalation in Raman Spectra

Doping is caused by both the EDL formation and intercalation in BLG and FLG. The doping from the EDL layer is distributed evenly between the graphene layers, causing a uniform blue shift of the G peak, and this doping effect increases linearly with applied bias. The G-peak shift from the EDL doping is exhibited at lower biases (±1V) in figure 2.3a, which looks similar to the G peak behavior in figure 2.2a. At higher biases, intercalation occurs and significantly increases the doping level. However, the intercalants do not enter all the van der Waals gaps at once. The intercalants instead form what are called staged intercalation compounds. These staged compounds are defined by a stage number, defined as the number of graphene host layers between each intercalant layer. For example, a stage-2 GIC has two layers of graphene between each intercalant layer, and a stage-1 GIC is fully intercalated with a layer of intercalants in every van der Waals gap. The stage number decreases as the number of intercalant layers increases, and each staged compound forms at a specific electrochemical potential. Therefore, the lower stage numbers form at higher applied biases (Dresselhaus & Dresselhaus, 2002; Ebert, 1984; Sole, Drewett, & Hardwick, 2014).

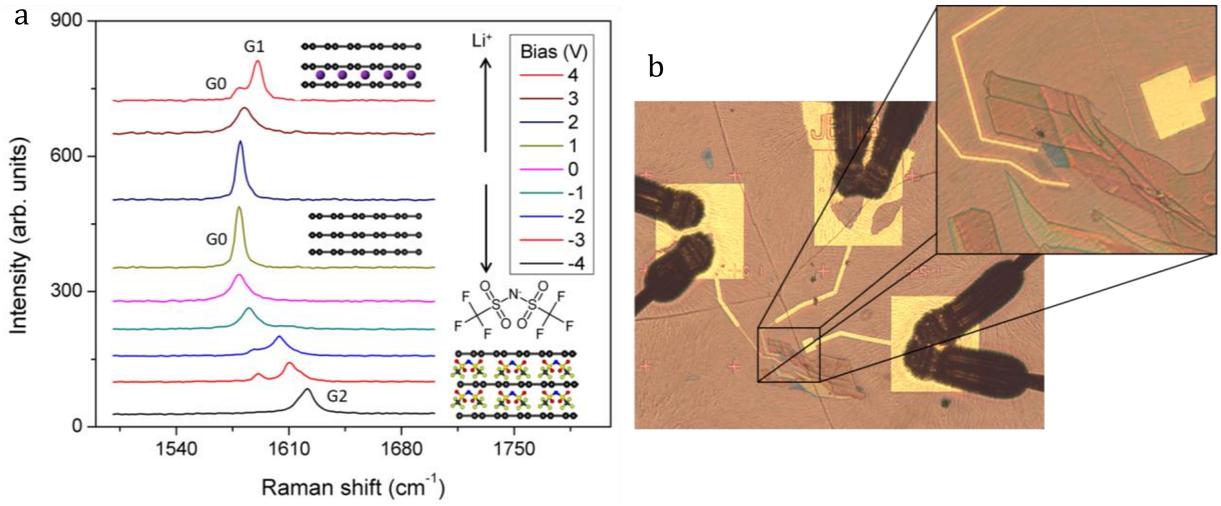

Figure 2.3: (a) G peak of few-layer graphene at different gate biases for an electrolyte field effect transistor device. The inset diagrams show the intercalation stages with the characteristic G peaks labelled as G0, G1, G2 (b) An optical image of the device used to collect the data for panel a.

In FLG, the intercalation products are limited to lower stage numbers. For example, trilayer graphene can only form stage-1 and stage-2 compounds as illustrated in figure 2.3a. One intercalant layer forms first, and then the second intercalant layer forms in the empty van der Waals gap at a higher applied bias. This staged intercalation causes the original G peak (G0) to split into other further blue shifted peaks (G1 & G2) because the intercalant layers only dope the neighboring graphene layers. The intercalated FLG also retains the high transparency of unintercalated FLG, which allows the laser light to pass through and undergo Raman scattering in all of the layers (Bao et al., 2014; Khrapach et al., 2012). Thus, the G0 peak corresponds to graphene layers not contacting any intercalant layers; the G1 peak corresponds to graphene layers in contact with one intercalant layer, and the G2 peak corresponds to graphene layers in contact with two intercalant layers as depicted in figure 2.3a (De Sanctis et al., 2017; W. Zhao et al., 2011).

Raman spectroscopy is a versatile tool for confirming the presence of intercalants and gathering information about the structure of the intercalation compound, but it has several limitations. The data acquired with Raman spectroscopy are spatially averaged over the laser spot, which is diffraction limited. The spectra displayed in figures 2.2 and 2.3 were obtained with a spot size of nominally one micrometer in diameter, and these spectra are a convolution of the Raman signals from the entire area illuminated by the laser spot. Another limitation of Raman spectroscopy is the lack of signal from some vibrational modes. Only centrosymmetric molecules and centrosymmetric crystal lattices have Raman active modes such as the G mode depicted in figure 2.2a. Also, structures with heavier elements are difficult to analyze with Raman spectroscopy because the Raman shifts corresponding to those vibrational modes are close to the laser line, which needs to be filtered out of the spectra. The Raman spectra of FLG has peaks that are well defined and separate from the laser line, which why the changes in the FLG spectra are commonly used to optically determine the intercalation products.

2.2 *In Situ* Scanning Transmission Electron Microscopy

Since Raman spectroscopy has several limitations and cannot provide information about the atomic structures within the intercalant layer, we also employ aberration-corrected scanning transmission electron microscopy (STEM) to examine the atomic structure of the intercalants. Aberration-corrected STEM is an essential tool for this job because it simultaneously provides real-time atomic resolution images *via* annular dark-field (ADF) detection and elemental characterization *via* electron energy loss spectroscopy (EELS).

2.2.1 Background on Scanning Transmission Electron Microscopy

The electron beam used for imaging during STEM is focused down to a sub-Ångstrom focal spot and scanned over the sample as depicted in figure 2.4a. Electrons scatter from the cores of the atoms when the electron beam is aligned with atomic columns in the material. Some of the electrons scatter at an angle, typically 50-200 mrad, and are collected by the ADF detector. The example ADF image shown in figure 2.4c is constructed by correlating the signal from the ADF defector with the position of the electron beam as it is scanned over the sample.

Other electrons scatter with smaller deflection angles but still interact with the cores of the atoms. This interaction excites the core electrons to higher energy levels and reduces the kinetic energy of the scattering electrons by the amount of energy required to generate the excitation. These scattered electrons are then collected in the EELS spectrometer, which separates the electrons by their kinetic energy. The EELS spectrum is produced by plotting the intensity of the signals in the spectrometer as a function of the kinetic energy lost from the scattered electrons. An example of an EELS spectrum is displayed in figure 2.4d. Each feature in the spectrum can be correlated to an atomic species due to the different amounts of energy required to generate core excitations in each element.

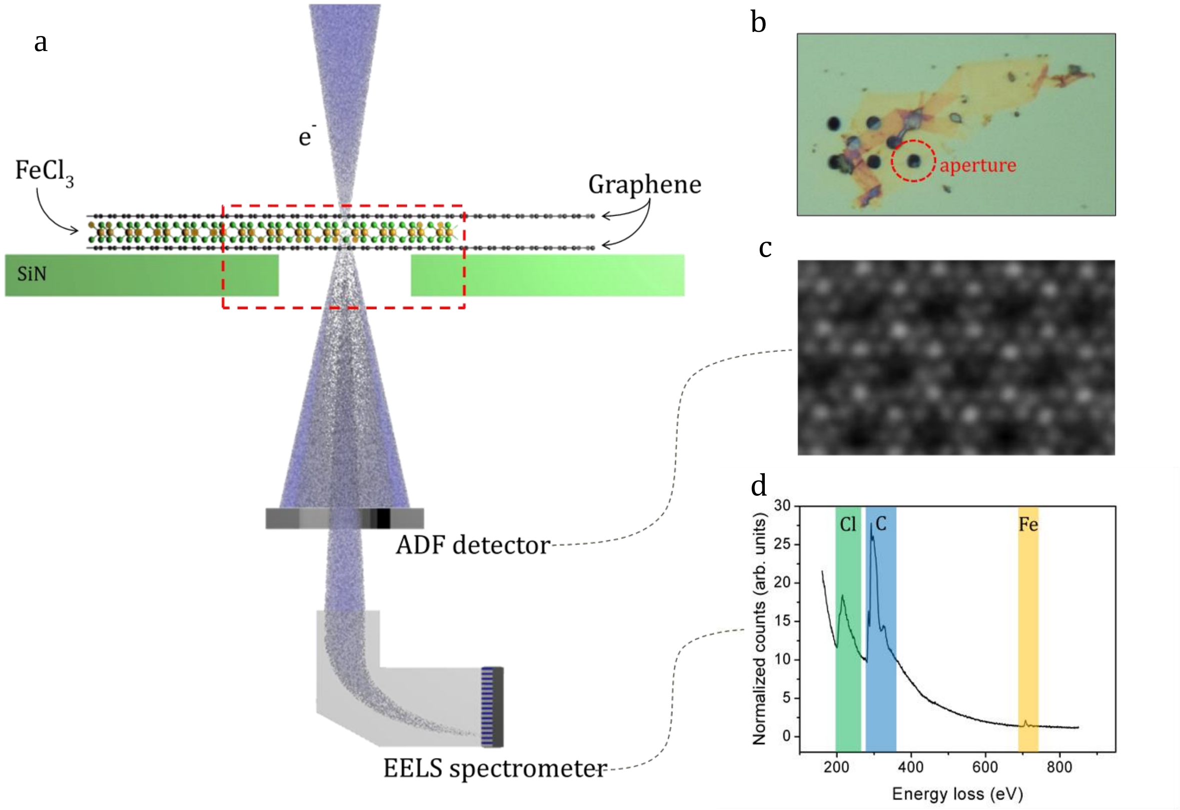

Figure 2.4: (a) Diagram of FeCl$_3$-BLG inside a STEM with EELS capabilities (b) Optical image of the same sample with a dotted red outline showing the region where STEM is performed (c) ADF image of the same sample (d) EELS of the same sample with labels on the signals for chlorine (green), carbon (blue), and iron (yellow) atoms.

2.2.2 Devices for *In Situ* Scanning Transmission Electron Microscopy

Devices for *in situ* STEM need to be suspended, pristine, and compatible with ultrahigh vacuum. To achieve atomic-resolution images, the electron beam must pass through the material without any interference from other atoms in the substrate or surface contaminates. We build the devices on Fusion E-chips$^{\text{TM}}$ from Protochips$^{®}$. The E-chips are silicon substrates with suspended silicon nitride membranes in the center and gold electrical leads that run to the membranes. The dimensions of these E-chips are designed to work with the Aduro^{TM} holder we use in the Nion UltraSTEM 100^{TM} microscope.

The first fabrication step is milling an aperture in the silicon nitride membrane for the electron beam to pass through when imaging. We use a Helios Nanolab G3 CX to mill two-micron apertures with a focused ion beam. We then use a viscoelastic transfer method to position the FLG over the aperture, and we then define electrodes from the E-chip leads to the FLG using electron beam lithography (EBL). These fabrication steps are illustrated in figure 2.5, and more details about the viscoelastic transfer method and EBL process are given in appendix A.

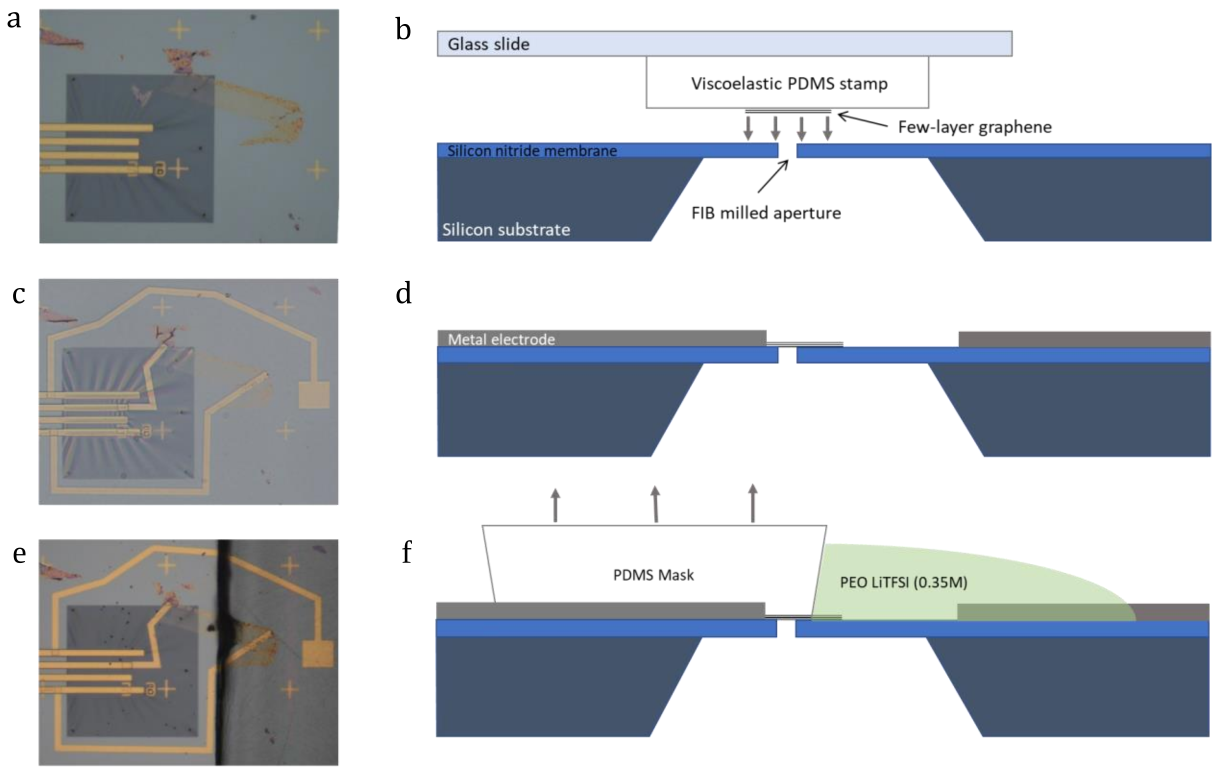

Figure 2.5: (a) Optical image of FLG transferred onto the membrane of a Protochips^{TM} E-chip (b) Schematic of the transfer process viewed from the side (c) Optical image of the same device after lithography (d) Schematic of the device after lithography viewed from the side (e) Optical image the device after depositing the polymer electrolyte (f) Schematic of the electrolyte deposition process viewed from the side.

The next step of fabrication is depositing the electrolyte, but we cannot simple drop cast the electrolyte like the device shown in figure 2.1. The electrolyte needs to cover part of the FLG without covering the aperture where we perform STEM. We achieve this electrolyte topography using a (polydimethylsiloxane) PDMS mask, positioning the PDMS mask over the FLG flake using the same transfer stage illustrated in figure A.1 (appendix A). The electrolyte is made by dissolving lithium bis(trifluoromethanesulfonyl)imide salt (LiTFSI) and polyethylene oxide (PEO) in a solvent (acetonitrile). We then deposit the electrolyte on the masked device and evaporate the solvent off by baking on a hot plate. More details about the electrolyte preparation protocol are given in appendix A. A picture of a finished device after depositing the electrolyte and removing the mask is shown in figure 2.5e.

The PEO LiTFSI polymer electrolyte is the same electrolyte used on the device in figure 2.3. This electrolyte shows consistent intercalation of both Li^+ and $TFSI^-$ when the entire FLG flake is covered in the electrolyte. However, the device performs differently when only part of the FLG flake is covered with the electrolyte: the electrolyte appears to migrate across the surface of the FLG rather than intercalate when sufficient bias is applied to the device. This migration of the electrolyte is exhibited in figure 2.6a. We hypothesize that this migration is caused by electrophoretic forces, the friction and attractive forces between charged ions and polarized polymer molecules that retards the motion of the ions. When a bias is applied to the device, the ions migrate through the polymer and attract some of the surrounding polymer molecules. At the edge of the polymer electrolyte there is still an electrostatic force on the ions but no more polymer for the ions to migrate through. However, the ions can continue to migrate if the surrounding polymer migrates along with the ions *via* the electrophoretic forces. The migration of the polymers with the ions avoids the additional work required to desolvate the ions (*i.e.* strip the polymer shell from the ions). If the electrochemical potential at which this migration occurs is lower than the potential required for intercalation, then intercalation will not occur because the concentration of ions at the electrolyte-FLG interface will decrease, thereby reducing the electrochemical potential of ions in the electrolyte.

To test this hypothesis, we used a different polymer for the electrolyte. The new polymer is made with a crosslinked copolymer. We mix poly(ethylene glycol) methyl ether methacrylate (PEGMA) and bisphenol A ethoxylate dimethacrylate (BEMA) with the LiTFSI salt and then crosslink the PEGMA and BEMA using a photo-initiator (2-hydroxy-2methylpropiophenone) and ultraviolet radiation (details about the electrolyte preparation protocol are given in appendix A). This new copolymer is mechanically more robust than the polyethylene oxide (PEO) polymer previously mentioned, and the covalent bonds between the polymer units resist the migration of polymers outside the defined electrolyte boundary (Kühne et al., 2017; Nair et al., 2012). We also create a physical barrier to prevent polymer migration by encapsulating the electrolyte in SiO_2 as illustrated in figure 2.6b.

An optical image of this device with the crosslinked copolymer electrolyte and SiO_2 barrier is displayed in figure 2.6c and does not show evidence of polymer migration. The Raman spectra of the device under bias are displayed in figure 2.6d and exhibit evidence of $TFSI^-$ intercalation when the device has negative bias applied to it. Although the Raman signal is weak due to lack of reflection from the substrate and additional noise is present due to background fluorescence from the silicon nitride, the G peak in figure 2.6d splits at -3V bias and resolves to one blue-shifted G peak with a Raman shift of ~1615cm^{-1} at -4V bias. These Raman signatures are similar to the signatures in figure 2.3a and suggest that the FLG is fully intercalated with

TFSI$^-$. This evidence supports the hypothesis that migration of the polymer electrolyte was preventing intercalation from occurring at the edge of the FLG under the electrolyte.

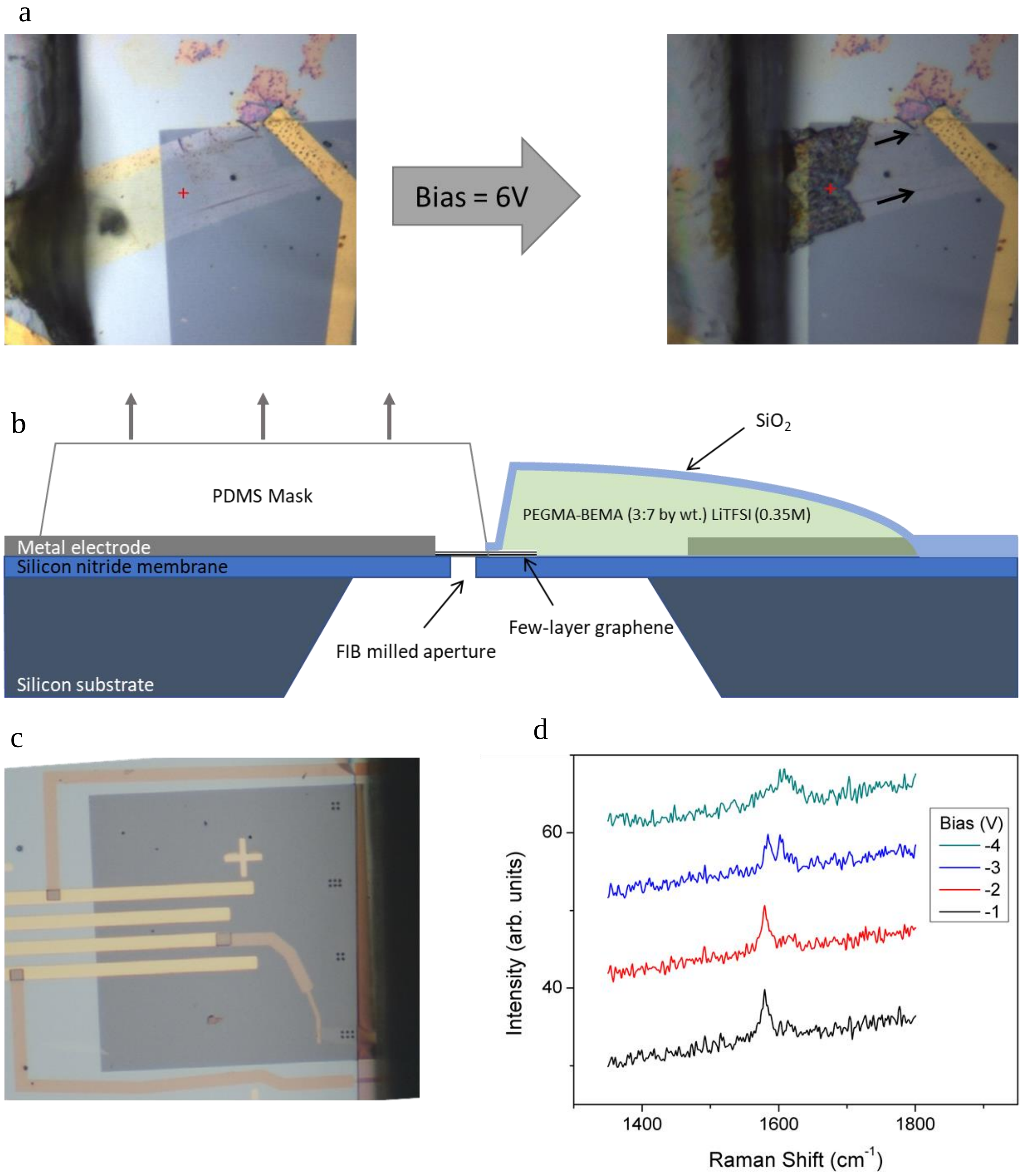

Figure 2.6: (a) Optical image of a device exhibiting migration of the polymer electrolyte (b) Schematic of the SiO_2 deposition to prevent polymer migration (c) Optical image of a device with SiO_2 covering the electrolyte as shown in panel b. (d) Raman spectra of the device in panel c displaying the G peak at different voltage biases.

2.2.3 *In situ* Scanning Transmission Electron Microscopy Experiments

We used STEM on the device displayed in figure 2.6c and other similar devices, but we unfortunately did not see any evidence of Li^+ or $TFSI^-$ intercalation in the ADF images or EELS spectra. However, a recent publication using the same device architecture and chemistry contains evidence for superdense ordering of lithium inside BLG *via in situ* STEM (Kühne et al., 2018). The researchers demonstrated that the lithium intercalated in BLG forms a close-packed structure that exceeds the density of lithium in fully intercalated stage-1 graphite. This discovery is potentially useful for developing energy storage applications in which FLG is implemented in novel intercalation battery electrode materials (Cohn, Share, et al., 2016; Lin, Wu, & Liu, 2018; Palumbo et al., 2019; Share et al., 2016; Zhang et al., 2017).

To this date though, this *in situ* STEM experiment has not been performed with $TFSI^-$ intercalation. The data collected from such an experiment would allow us to precisely determine the orientation, conformation, and intermolecular ordering of the $TFSI^-$. Similar experiments could also be done with other common polyatomic intercalants, such as hexafluorophosphate (PF_6^-) and perchlorate (ClO_4^-), which would be important information for developing new dual-graphite cell batteries (Beltrop et al., 2017; Fan, Qi, & Wang, 2017; Fan, Qi, Yoshio, & Wang, 2017; Read et al., 2014; Rothermel et al., 2014).

The Raman spectroscopy data that we have collected suggest that $TFSI^-$ intercalation is possible with the same device architecture, but the STEM experiments showed no evidence of intercalation with devices operating at the same biases as the Raman spectroscopy experiments. The reason for this discrepancy may be that the device was damaged before the STEM experiment was performed. We hypothesize that the baking protocol for STEM samples changed the composition of the electrolyte before the device entered the microscope. After the device is loaded into the STEM sample holder, it must be baked at a temperature of at least 80 ^{o}C under vacuum to remove residual moisture and hydrocarbons. The electrolyte should be stable up to 100 ^{o}C according to previous thermal stability tests (Nair et al., 2012), but the specific composition of the electrolyte on our *in situ* devices may have varied enough to lower the thermal stability. This hypothesis is supported by Raman spectroscopy completed on the devices after the attempted STEM experiments, which did not display evidence of intercalation like the initial Raman spectra that were taken before STEM.

Successful *in situ* STEM experiments will likely require doing thermal stability tests on the electrolyte using methods such as thermogravimetric analysis to ensure the devices function properly after the required baking protocol. Additionally, the electrical contacts on the FLG can be used to monitor for the presence of intercalants by measuring the resistivity of the FLG, which can be executed with the device in the microscope. These changes to the experiment and device testing are important considerations for future work on this project.

2.3 Chemical Vapor Transport Method of Intercalation

Electrochemical intercalation is a useful tool for controlling the intercalation process in real time, but as discussed in the previous section, it requires extensive fabrication and testing to intercalate FLG electrochemically for STEM experiments. A more straightforward intercalation method for STEM experiments is chemical vapor transport (CVT). This method involves sealing the FLG and intercalant material in a glass reaction vessel under vacuum and heating the reaction vessel to evaporate the intercalants. The gaseous intercalants then fill the reaction vessel and spontaneously intercalate into the FLG at the other side as illustrated in figure 2.7. The FLG sample for STEM experiments is prepared on a silicon nitride membrane with 2 μm apertures (see figure 2.7a) using the viscoelastic transfer method described in appendix A. No electrical contacts or electrolyte are used in this method, and the STEM experiment is done *ex situ*. Additionally, the stage number can be controlled by varying the temperature difference between the two sides of the reaction vessel (Dresselhaus & Dresselhaus, 2002).

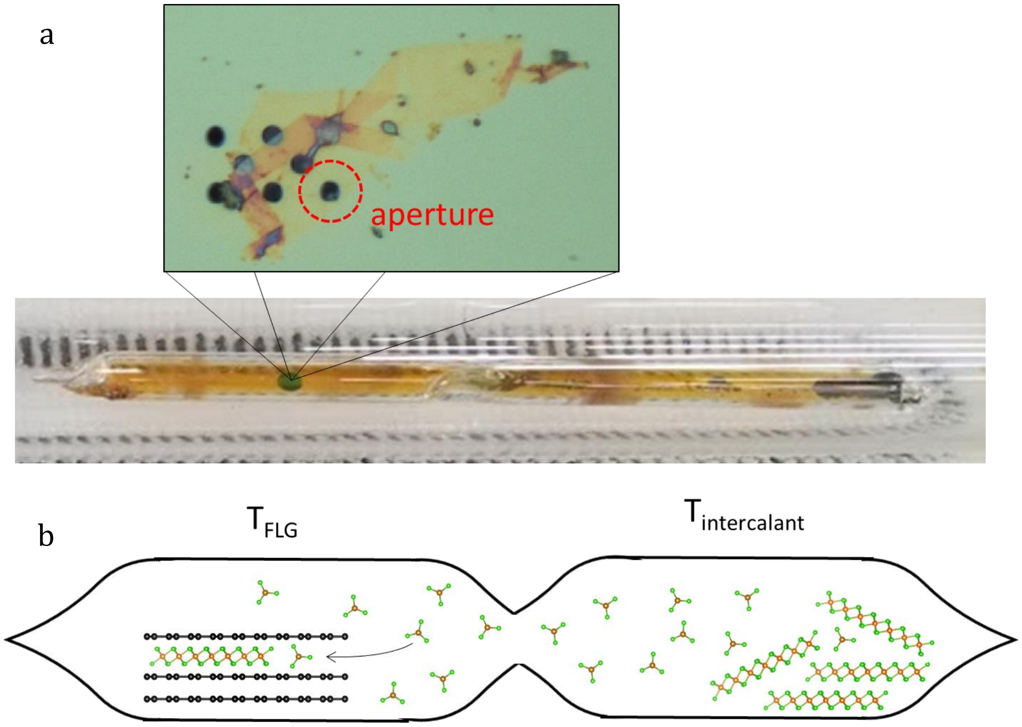

Figure 2.7: (a) Optical image of the reaction vessel used for the CVT intercalation method and a magnified image of the FLG sample inside (b) A diagram of the reaction vessel showing the intercalation process.

2.3.1 Thermodynamics of Intercalation *via* Chemical Vapor Transport

The reaction process for CVT intercalation is written as:

$$\mathrm{Int(s)} \rightarrow \mathrm{Int(g)} \tag{1}$$

$$\mathrm{Int(g)} + \mathrm{xC(s)} \rightarrow \mathrm{C_xInt(s)} \tag{2}$$

The intercalant species is represented by Int in the above equations. The carbon in the FLG is represented by C, and x is the stoichiometric ratio between the carbon atoms and intercalant molecules. Equation 1 describes the sublimination/evaporation of the intercalant material in one side of the reaction vessel at temperature T_{int}, and equation 2 describes the intercalation reaction in the other side of the reaction vessel at temperature T_{FLG}. The temperature at the intercalant side of the reaction vessel (T_{int}) must be high enough to vaporize the chosen intercalant material, and the FLG side must be at a higher temperature to prevent recrystallization of the intercalant material before intercalation can occur. The precise temperature to use at the FLG side (T_{FLG}) is not tri*via*l though. It is important to use a T_{FLG} that will result is a low stage number because only low stage numbers are possible in FLG. For example, only stage 1 intercalation is possible in BLG as mentioned in the previous sections on electrochemical intercalation.

We use the Gibbs free energy for these processes to determine the spontaneity of the reaction and resulting stage number of the intercalation products as a function of T_{FLG}. The change in Gibbs free energy for equation 1 at the intercalant side of the reaction vessel (ΔG_{int}) is given by:

$$\Delta \mathrm{G}_{\mathrm{int}} = \Delta_{\mathrm{v}}\mathrm{H} - \mathrm{T}_{\mathrm{int}}\Delta_{\mathrm{v}}\mathrm{S} \qquad (3)$$

This is a typical ΔG for a vaporization process in which the enthalpy of vaporization ($\Delta_v H$) and change in entropy ($\Delta_v S$) are always positive. Therefore, the process is spontaneous if $\mathrm{T}_{\mathrm{int}} > \frac{\Delta_{\mathrm{v}}\mathrm{H}}{\Delta_{\mathrm{v}}\mathrm{S}}$, and thus ΔG_{int} is a small constant since we use the minimum T_{int} for vaporization. The change in Gibbs free energy for equation 2 at the FLG side of the reaction vessel (ΔG_{FLG}) is given by:

$$\Delta \mathrm{G}_{\mathrm{FLG}}(\mathrm{T}_{\mathrm{FLG}}, \mathrm{x}) = \Delta \mathrm{H}(\mathrm{x}) - \mathrm{T}_{\mathrm{FLG}}\Delta S(\mathrm{x}) \qquad (4)$$

This ΔG is a function of the temperature (T_{FLG}) and the stoichiometric ratio (x), which corresponds to the stage number. It is a function of T_{FLG} because this temperature is varied to change the stage number of the intercalation product, and it is a function of x because the different staged intercalation compounds have different enthalpies and entropies of formation.

We predict how the Gibbs free energy will change for intercalated FLG by looking at how the enthalpy and entropy change in intercalated graphite. Calorimetric data from graphite intercalated with alkali metals exhibit negative enthalpy and entropy of formation, and as more intercalants enter the graphite (*i.e.* x and the stage number decrease), the enthalpy becomes less negative and entropy becomes more negative (Dresselhaus & Dresselhaus, 2002; Hennig, 2007; Novikov & Vol'pin, 1971; Rüdorff, 1959; Salzano & Aronson, 1965, 1966). These data combined with equation 4 suggest that a higher T_{FLG} will result in a higher stage number for the intercalation product, which is observed in graphite for various intercalant species (Dresselhaus & Dresselhaus, 2002; Hooley, 1973; Hooley & Bartlett, 1967; Nixon & Parry, 1968; Rudorff & Zeller, 1955; Salzano & Aronson, 1965, 1966). Therefore, the optimal T_{FLG} for intercalating FLG or BLG is a temperature close to T_{int} without being less than T_{int}. This optimal temperature allows intercalation of FLG and BLG, which requires low stage numbers, without allowing recrystallization of the intercalant material at temperatures below T_{int}.

2.3.2 Intercalant Materials for Chemical Vapor Transport Intercalation

We must also choose intercalant species that can form stage 1 compounds *via* CVT intercalation if we want to be able to intercalate BLG. For example, stage 1 compounds of sodium and bromine do not have a negative ΔG for any temperature above T_{int}, which means that the sodium/bromine will recrystallize/liquify before intercalation can occur when attempting CVT intercalation (Aronson, 1963; Asher, 1959; Axdal & Chung, 1987; Dresselhaus & Dresselhaus, 2002). The other alkali metals work well for CVT intercalation, but the resulting intercalation compounds are very reactive and not air stable. We use iron(III) chloride ($FeCl_3$) as the intercalant material for *ex situ* STEM experiments. Few-layer graphene intercalated with $FeCl_3$ is stable in ambient conditions over months, resists degradation by common solvents, and has both high conductivity and high optical transparency (Wehenkel et al., 2015; W. Zhao et al., 2011). These properties invite potential applications for energy storage, transparent conductors, and heat spreaders (Khrapach et al., 2012; Qi et al., 2015). Additionally, $FeCl_3$ can form stage 1 compounds, which allows for intercalation in BLG (Hooley, 1973; Hooley & Bartlett, 1967; Wehenkel et al., 2015). Performing STEM on BLG intercalated with $FeCl_3$ lets us examine a single layer of intercalants and test our hypothesis about whether polyatomic intercalants form crystalline monolayers.

CHAPTER 3

Atomic Structure of $FeCl_3$ Intercalated in Few-layer Graphene

3.1 Background on $FeCl_3$ Intercalated Few-layer Graphene

Few-layer graphene intercalated with iron chloride (FLG-$FeCl_3$) is a particularly interesting example of a few-layer intercalation compound, although $FeCl_3$-intecalated BLG (BLG-$FeCl_3$) has received limited attention (Wehenkel et al., 2015). Experiments have found that the presence of $FeCl_3$ causes decoupling of the carbon layers, resulting in a graphene-like band structure and induces a very large carrier density up to 10^{14} cm^{-2} in the graphene sheets (corresponding to a Fermi level shift as large as 1.3 eV below the Dirac point) (W. Zhao et al., 2011). Highly doped graphene and intercalated graphite are interesting for the study of exotic superconductivity as mentioned in chapter 1 (Al-Jishi, 1983; Nandkishore, Levitov, & Chubukov, 2012). In addition, it has been suggested that FLG-$FeCl_3$ develops an interesting magnetic structure with ferromagnetic order inside each $FeCl_3$ layer and antiferromagnetic coupling between the neighboring layers (Bointon et al., 2015; Li & Yue, 2013). Such order is especially interesting in the context of the recent interest in two-dimensional magnetism (Gibertini, Koperski, Morpurgo, & Novoselov, 2019; Gong et al., 2017; Gong & Zhang, 2019; B. Huang et al., 2018; Jiang, Shan, & Mak, 2018; McGuire, Dixit, Cooper, & Sales, 2015).

While multiple experiments addressed the macroscopic properties of FLG-$FeCl_3$, its microscopic structure remains virtually unknown and the possibility that multiple intercalant structures form has not been adequately explored. Electron diffraction and powder XRD data from $FeCl_3$-GICs suggest that within each van der Waals gap the $FeCl_3$ molecules form a honeycomb lattice similar to bulk $FeCl_3$ (Cowley & Ibers, 1956; Dresselhaus & Dresselhaus, 2002). XRD, however, being a spatially averaged technique, is not sensitive to several possibilities. For example, intercalant layers in FLG may have layer-number dependent properties, as is known to occur in the lithium intercalation process (Hui et al., 2016). Such properties should be studied to understand the predicted antiferromagnetic coupling between neighboring $FeCl_3$ layers (Bointon et al., 2015). Previous research also demonstrates that $FeCl_3$ is converted to $FeCl_2$ in a reducing environment, but the published work on the stability of FLG-$FeCl_3$ does not consider the possibility of $FeCl_2$ formation (Dresselhaus & Dresselhaus, 2002). Lattice defects in FLG-$FeCl_3$, if present, have not so far been investigated by any means, but are expected to strongly scatter the carriers in graphene layers, thereby limiting applicability of FLG-$FeCl_3$ in electronics. The presence of defects should also affect the dynamics of the intercalation process and thus be critical for energy storage applications.

The samples were fabricated using the CVT method of intercalation described in chapter 2. Details about the protocol used for CVT intercalation of $FeCl_3$ are given in appendix A. Bilayer graphene and few-layer graphene were transferred onto holes (2 μm diameter) in silicon nitride membranes using the viscoelastic transfer described in appendix A. The samples were vacuum sealed in borosilicate ampoules with anhydrous $FeCl_3$ and then transferred to a tube furnace for the intercalation reaction. After intercalation, the samples were washed with deionized water to remove any adsorbed $FeCl_3$ that could interfere with imaging of the intercalated $FeCl_3$. Raman spectroscopy was performed before and after intercalation to confirm the presence of $FeCl_3$, which is evidenced by new blue-shifted G peaks (W. Zhao et al., 2011). Additional experimental details about sample characterization are also given in appendix B.

3.2 Atomic Structure of $FeCl_3$ Monolayer

Aberration-corrected STEM was used to investigate the atomic structure of the resulting intercalants. Atomic-resolution images were obtained using an ADF detector, and the elemental composition was confirmed using EELS, as illustrated in figure 2.4, where we show data for a $FeCl_3$-BLG sample. While intercalated iron and chlorine are clearly resolved, carbon atoms are barely visible as the ADF signal strength is roughly proportional to the square of the atomic number. Thus, the Fe and Cl signals are roughly nineteen and eight times stronger, respectively, than the carbon signals. A key result of this investigation is that we were able to identify both $FeCl_3$ and $FeCl_2$ in adjacent regions, which indicates that $FeCl_3$ molecules can undergo reduction within the van der Waals gap of BLG. We first present the data and analysis for $FeCl_3$ intercalants. The pertinent ADF image in figure 3.1a exhibits a 2D honeycomb structure. This structure is the same as in bulk $FeCl_3$ with each iron atom bonded to six chlorine atoms in an octahedral geometry, as shown in figure 3.1c. The carbon atoms can be seen faintly inside the holes of the $FeCl_3$ honeycomb lattice displayed in figure 3.1a, although the contrast is much lower than that of the chlorine and iron atoms. In areas where there is incomplete intercalation, as seen in figure 3.1d, the intercalants form islands that are separated from neighboring unintercalated regions by an atomically sharp boundary. This sharpness is due to in-plane covalent bonds between the iron chloride molecules in the intercalant layer.

To unambiguously determine the position of each atomic species with STEM simulations, atomic positions optimized by density-functional-theory (DFT) calculations and the experimental beam parameters were used as inputs to the QSTEM software package to create simulated ADF images, displayed in figure 3.1b for comparison to the experimentally obtained images. There is good agreement between the ADF image and STEM simulation. The measured

$FeCl_3$ lattice constant of 0.61±0.01 nm agrees with the theoretical value of 0.60 nm. These data demonstrate that the intercalated $FeCl_3$ forms a 2D material in between the graphene layers.

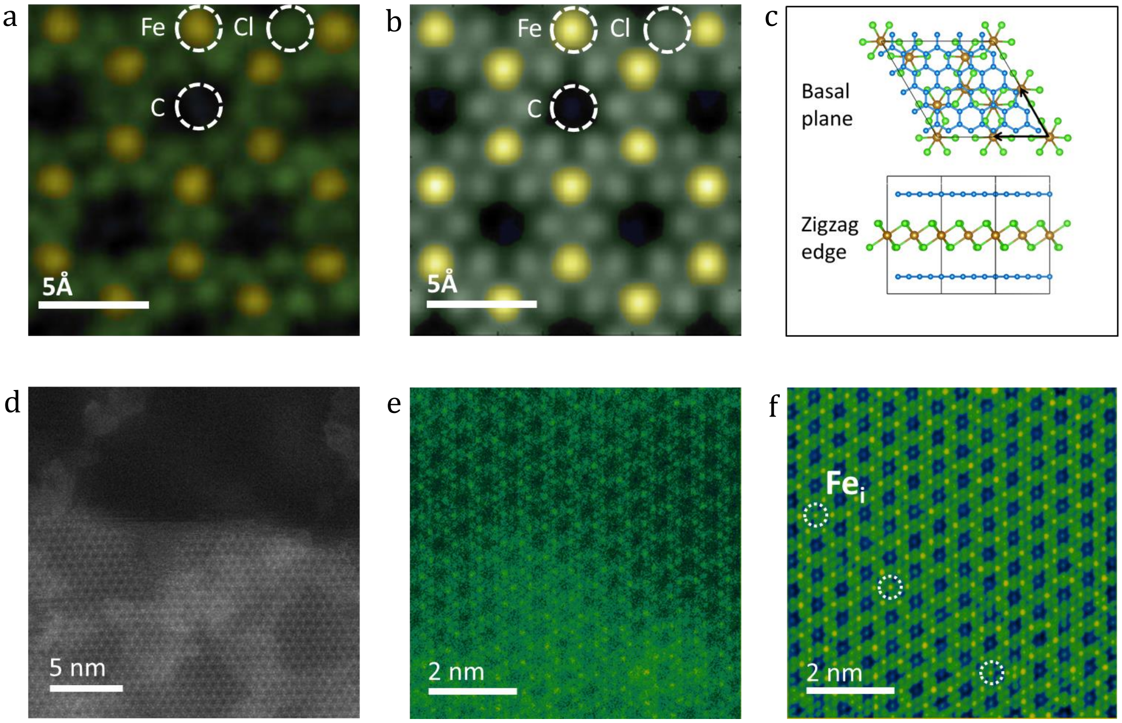

Figure 3.1: (a) Colorized ADF image of $FeCl_3$-BLG (b) Colorized QSTEM simulation of $FeCl_3$-BLG (c) Diagram of $FeCl_3$-BLG with black arrows displaying the primitive lattice vectors of $FeCl_3$ (d) ADF image of intercalation boundary (e) Unfiltered ADF image of $FeCl_3$-BLG used for PCA filtering (f) Same image as in e, but filtered using components 2-10 of the PCA. Iron interstitial defects are highlighted by white dotted outlines as visible (the colors are determined by a color scale ranging from dark blue to yellow).

In order to better resolve carbon atoms and reduce surface contamination effects, we filtered the original data, shown in figure 3.1e, using principal component analysis (PCA) (Ovchinnikov et al., 2018; Somnath et al., 2018). We noticed that the first PCA component corresponds primarily to the surface contamination and the higher order components (>10) correspond to background noise in the image. We therefore plotted the components 2 through 10 in figure 3.1f. The three types of atoms present in the samples are visible in the images. While the background is dark blue, iron atoms appear yellow, chlorine atoms – green, and carbon atoms – light blue. These light blue spots are separated by 0.57±0.01 nm, which corresponds to four times the carbon-carbon bond in graphene, and sometimes appear off center or as dumbbells inside the hexagons of the $FeCl_3$ lattice. These observations further confirm the source of the light blue spots as the carbon lattice and not an artifact from the $FeCl_3$ structure, which would have similar hexagonal symmetry. The location of the carbon atoms indicates that the carbon lattice and $FeCl_3$ lattice are aligned with each other in this sample. The PCA filtering also displays interstitial iron atoms in the $FeCl_3$ hexagons. While interstitial iron can be seen on the left-center edge of the unfiltered image, figure 3.1e, the removal of the surface contamination in the image makes it clear that several such interstitials occur in this section of the sample. Such additional interstitial iron atoms at non-regular lattice sites are likely to impact the magnetic ordering properties of $FeCl_3$-intercalated FLG (Bointon et al., 2015).

3.3 Alignment of Multiple $FeCl_3$ Monolayers

We also imaged intercalated FLG with thicknesses of four to six graphene layers to study the relative angular alignment of $FeCl_3$ monolayers sandwiched between successive layers of graphene and test whether a superposition of $FeCl_3$ and $FeCl_2$ layers needs to be invoked to reproduce the images. The ADF images in figures 3.2 & 3.3 reveal only $FeCl_3$ layers with different degrees of alignment for different samples. The first sample shown in figure 3.2g exhibits complete angular alignment of the $FeCl_3$ layers, observed as coincident ADF signal from the atoms in each layer. The stacking configuration is inferred by comparing the ADF image with STEM simulations of bilayer and trilayer $FeCl_3$ and $FeCl_2$ in different stacking configurations. Two and three layers were used since the sample had approximately four to six layers of graphene, determined by atomic force microscopy, and the Raman spectrum of the sample after intercalation indicates partial intercalation. These characterization details are given in appendix B.

3.3.1 Stacking Configuration of Aligned $FeCl_3$ Monolayers

The best agreement between the ADF image and STEM simulation is for ABC stacking of $FeCl_3$ when comparing AB, ABA, and ABC stacking configurations of both $FeCl_3$ and $FeCl_2$. The STEM simulation for ABC-stacked $FeCl_3$ is shown in figure 3.2c, while the simulations for the other stacking configurations can be found in figure 3.2a & 3.2b. It is also worth noting that the angular detection range of the ADF detector is essential for interpreting the image correctly with STEM simulations. Only a slight reduction of the detection range used in the simulations produces significantly different simulated images as seen in figures 3.2e-f. The correct experimental detection range is used in figures 3.2a-c.

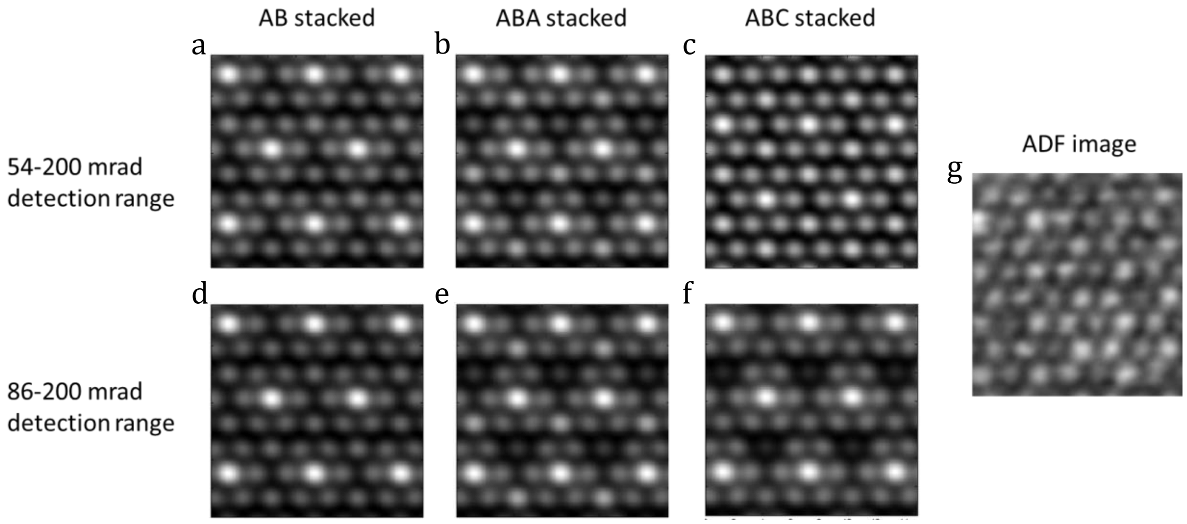

Figure 3.2: QSTEM simulations of (a) AB stacked $FeCl_3$ with 54-200mrad detection range (b) ABA stacked $FeCl_3$ with 54-200mrad detection range (c) ABC stacked $FeCl_3$ with 54-200mrad detection range (d) AB stacked $FeCl_3$ with 86-200mrad detection range (e) ABA stacked $FeCl_3$ with 86-200mrad detection range (f) ABC stacked $FeCl_3$ with 86-200mrad detection range (g) ADF image of $FeCl_3$ intercalated FLG.

3.3.2 Angular Alignment of $FeCl_3$ Monolayers

The second sample exhibits small angles of rotation between the intercalant layers, producing a moiré pattern in the ADF image displayed in figure 3.3a. The relative angles between each monolayer were determined from the fast Fourier transformation (FFT) of the ADF image. The FFT of the second sample, shown in figure 3.3b, displays sharp Fourier peaks in a hexagonal pattern due to the hexagonal structure of the crystal basis for $FeCl_3$. Each layer of $FeCl_3$ has a distinctive set of Fourier peaks, and the relative angle between the layers can be observed from the angles between those Fourier peaks. Three distinct sets of peaks can be seen in figure 3.3b with angles of 0º, 3.0º, and 5.5º. Given these angles, the lattice parameter of the moiré pattern ($a_{moiré}$) can be calculated using the following equation, which is derived in appendix D:

$$a_{moiré} = \frac{a}{\sqrt{2(1-\cos\theta)}} \tag{5}$$

where a is the lattice parameter of the $FeCl_3$ measured from the ADF image and θ is the relative angle between each layer measured from the FFT. Using the values of 3.0º and 2.5º in equation 5, the moiré lattice parameter is 12nm and 14nm respectively. The moiré patterns for these angles cannot be seen in the ADF image as they are too large for the size of the image, but 5.5º gives a moiré lattice parameter of 6.3 nm, which agrees with the measured moiré lattice parameter, 6.2±0.1 nm, seen in 9a.

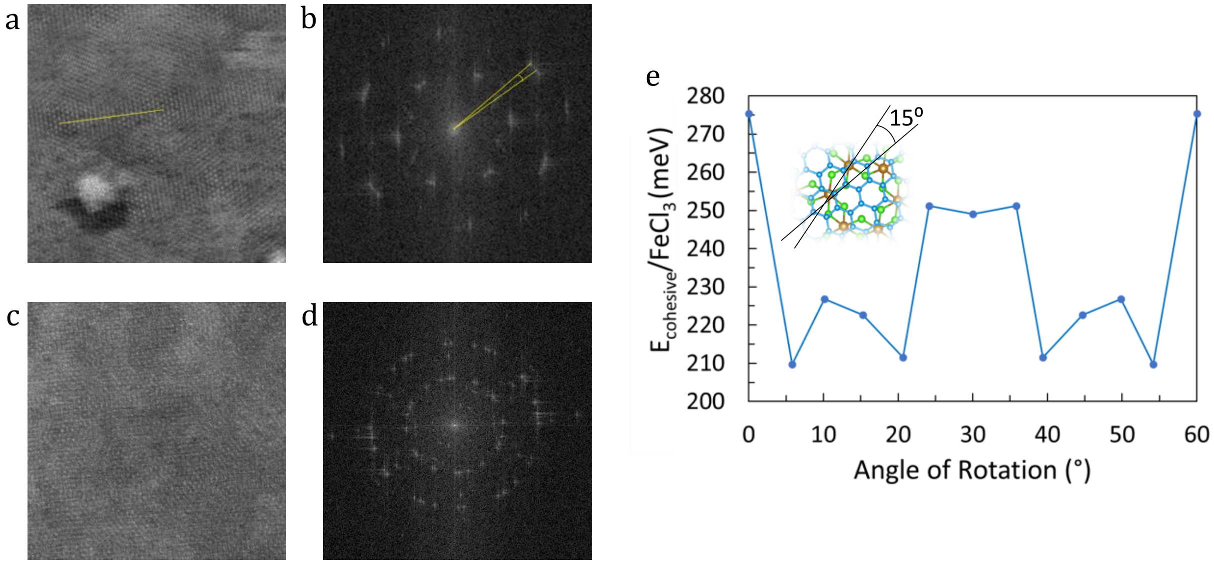

Figure 3.3: (a) ADF image of nearly aligned ABC stacked $FeCl_3$, where the yellow line indicates the length (6.2±0.1 nm) of the moiré lattice parameter (b) FFT of panel a, where the yellow lines indicate the angle (5.5°) between neighboring $FeCl_3$ layers (c) ADF image of $FeCl_3$ with uncorrelated stacking (d) FFT of panel d (e) Cohesive energy per $FeCl_3$ unit as a function of relative angle.

The third sample exhibits angles between $FeCl_3$ layers as large as 44° measured in the FFT (figure 3.3d) that corresponds to a_{moire} of 0.81 nm, close to the lattice parameter of $FeCl_3$ (0.607 nm). There are also at least six distinct sets of Fourier peaks spread across the 44° creating an FFT that resembles that of a polycrystal. The ADF image for this sample (figure 3.3c) appears disordered due to the number of layers and wide range of angles, but faint moiré patterns can still be seen from the layers of $FeCl_3$ that have small relative angles to each other, which correspond to moiré-pattern lattice parameters on the order of nanometers.

To gain insight into the source of the observed moiré patterns and apparent polycrystalline structure, we calculated the interlayer cohesion energetics as a function of twist angle between $FeCl_3$ and graphene, as shown in figure 3.3e. For the calculated angles, we find that there is a global energy minimum at 0°/60° and additional local energy minima at 10°, 25°, 35°, and 50°. However, the overall range of energies is only 65 meV per $FeCl_3$ unit. That energy range is significantly smaller than the available thermal energy (~6kT = 300 meV per $FeCl_3$ unit) suggesting that patches can nucleate with essentially any relative angle. Although bulk $FeCl_3$ orders with a relative AB stacking between layers, the presence of a graphene layer between two layers of $FeCl_3$ renders the two $FeCl_3$ stacking configurations degenerate. This result implies that in addition to the presence of relative twist angles between intercalant layers, the layers may also undergo relative shifts in origin, as previously suggested by X-ray diffraction studies on bulk intercalant structures (Cowley & Ibers, 1956).

CHAPTER 4

Other Atomic Structures Formed from $FeCl_3$ Intercalation

4.1 Atomic Structure of $FeCl_2$ Monolayer

We now turn to the region of the intercalant structure that is different from the honeycomb structure described in chapter 3, which we identify as $FeCl_2$. The pertinent ADF image is shown in figure 4.1e. This structure looks similar to a monolayer of $FeCl_3$ (figure 4.1a) but with an additional iron atom in the holes of the honeycomb lattice, signifying a change in stoichiometry from $FeCl_3$ to $FeCl_2$. Comparison of this structure to a STEM simulation of monolayer $FeCl_2$ in figure 4.1f exhibits good agreement, with an experimental lattice parameter of 0.350±0.005 nm compared to the theoretical value of 0.347 nm.

4.1.1 Comparison of $FeCl_3$ and $FeCl_2$ Monolayers

The atomic structures of $FeCl_3$ and $FeCl_2$ are shown in figure 4.1c and 4.1g. The ADF image in figure 4.1e displays good qualitative and quantitative agreement with the STEM simulation in figure 4.1f. There should only be one layer of iron chloride since there is only one interlayer region to intercalate in BLG. However, AB-stacked $FeCl_3$ looks quantitatively similar to $FeCl_2$. Fortunately, these two structures can be differentiated by the apparent lattice parameter in the ADF image. The lattice parameter for $FeCl_2$ is 0.347 nm, and the lattice parameter for AB-stacked $FeCl_3$ is 0.701nm. The measured lattice parameter of 0.350±0.005 nm is clear evidence that the other lattice structure in figure 4.1e is indeed $FeCl_2$.

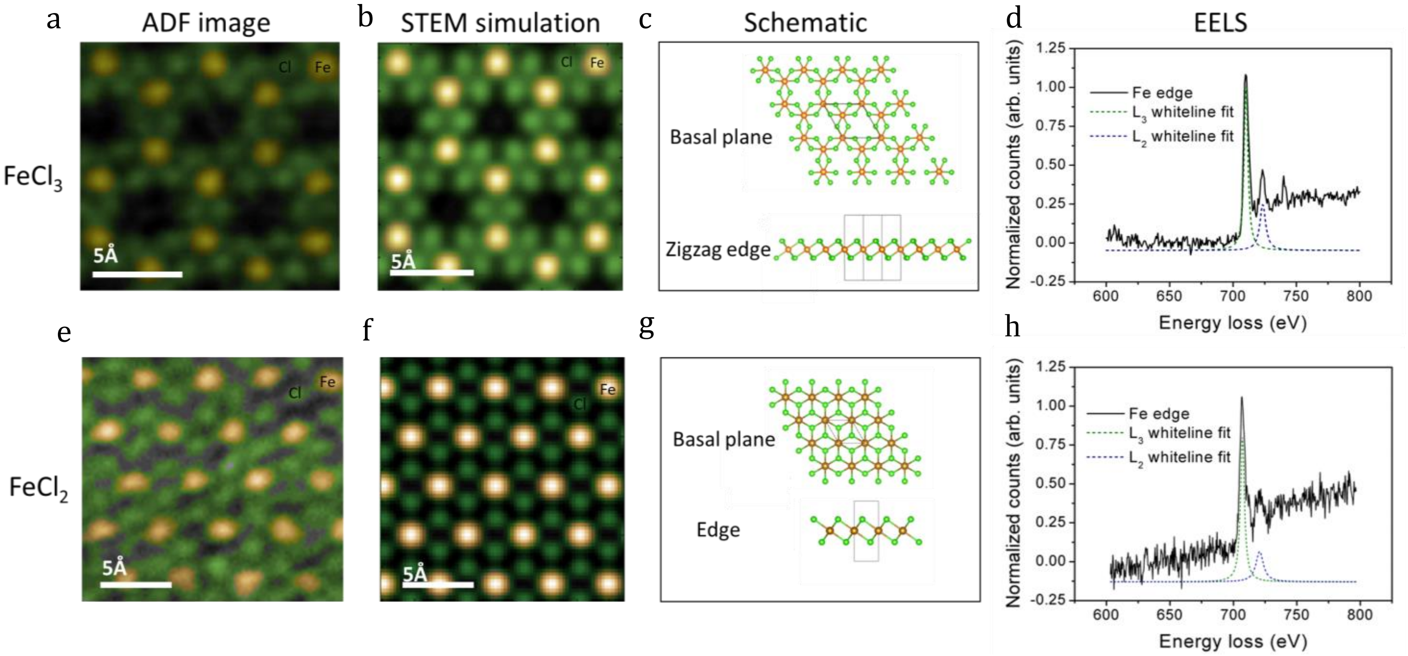

Figure 4.1: (a) ADF image of an intercalated FeCl$_3$ monolayer (b) QSTEM simulation of a FeCl$_3$ monolayer (c) Diagram of monolayer FeCl$_3$ (d) EELS spectra of the area shown in panel a with Lorentzian fits of the L$_3$ (dashed green) and L$_2$ (dashed blue) white-lines (e) ADF image of an intercalated FeCl$_2$ monolayer (f) QSTEM simulation of a FeCl$_2$ monolayer (g) Diagram of monolayer FeCl$_2$ (h) EELS spectra of the area shown in panel e with Lorentzian fits of the L$_3$ (dashed green) and L$_2$ (dashed blue) white-lines.

4.1.2 Electron Energy Loss Spectroscopy of Iron Atoms

We further probed the same region by EELS, which is sensitive to the iron oxidation state. We focus on spectral features corresponding to iron core electron excitations, highlighted yellow in figure 2.4d. These features include a step-like edge and Lorentzian-shaped peaks, referred to as white-lines, shown in figures 4.1d & 4.1h for FeCl$_3$ and FeCl$_2$ respectively. The ratio of the L$_3$ and L$_2$ white-line intensities is used to differentiate between Fe^{2+} and Fe^{3+} species, which have L$_3$/L$_2$ intensity ratios of 4.0 and 5.5 respectively (Lee, Zhou, Idrobo, Pennycook, & Pantelides, 2011). Experimentally, we determined that ratio using both Lorentzian fits as well the analysis of the second derivative of the data as described in appendix D (Lee et al., 2011). Both methods yield the ratio of 4±1, consistent with the structure being FeCl$_2$. The literature on intercalation of bulk graphite with $FeCl_3$ demonstrates that $FeCl_2$ cannot be intercalated on its own, but the $FeCl_3$ can be reduced to $FeCl_2$ after intercalation into the graphite (Dresselhaus & Dresselhaus, 2002). Given this evidence in the literature, we suggest that the $FeCl_3$ is reduced to $FeCl_2$ after the intercalation reaction. This happens due to the presence of a reducing agent, which could be hydrocarbon contaminants and hydrogen formed from other chemical reactions during the intercalation process.

4.2 Formation of FeOCl

Finally, we observe the formation of a new monolayer, displayed in figure 4.2a, that appears at the edge of the intercalated $FeCl_3$ monolayers in $FeCl_3$-BLG when exposed to the electron beam under STEM imaging conditions with 60 kV accelerating voltage. Such monolayers are never seen at the beginning of STEM imaging and cannot affect the interpretation of our Raman results that are recorded before STEM. This new monolayer forms a rectangular lattice composed of iron, chlorine, and oxygen as shown by EELS in figure 4.2b. The constituent components and lattice shape suggest that the compound is iron oxychloride (FeOCl), a material that has previously been described in bulk layered form (Hwang, Li, Lee, Lynn, & Wu, 2000; Lind, 1970). The identification of the material is corroborated in figure 4.2c by an overlay of the FeOCl monolayer atomic structure and experimental ADF image. The creation of this novel monolayer in the $FeCl_3$-intercalated bilayer system suggests the ability to engineer additional interesting materials and structures after the initial synthesis. More specifically, the microscope's electron beam is in effect used to "process" intercalants and convert them into new structures.

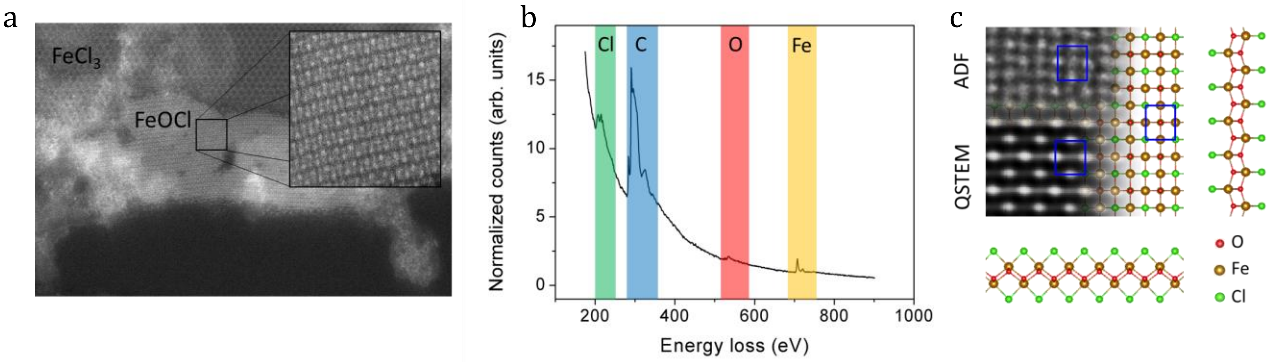

Figure 4.2: (a) ADF image of the edge of the FeCl$_3$ monolayer after it has been irradiated during imaging. The new rectangular structure that is visible is interpreted as FeOCl. (b) EELS of the same region (c) ADF image along with QSTEM simulation of FeOCl.

CHAPTER 5

Doping Effects of $FeCl_3$, $FeCl_2$, and Other Intercalants

5.1 Resonance-Raman Spectroscopy to Determine Doping Levels

We find further evidence for the coexistence of $FeCl_3$ and $FeCl_2$ regions in $FeCl_3$-BLG in their effects on the carrier density in graphene. The carrier density in graphene, as well as its proxy, the position of the Fermi energy relative to the Dirac point, were probed *via* Raman spectroscopy. Before intercalation, the Raman G mode peak is at 1582 cm^{-1}. After intercalation, the G peak splits into three peaks – G0, G1, and G2 at 1586 cm^{-1}, 1614 cm^{-1}, and 1626 cm^{-1} respectively. These spectral peaks are displayed in figure 5.1a. Since the spectral position of the G mode is indicative of the local carrier density in graphene, such splitting is consistent with the presence of regions with three distinct carrier densities within the diffraction-limited laser spot on the sample (Froehlicher & Berciaud, 2015; Lazzeri & Mauri, 2006). With its spectral position within 4 cm^{-1} from the G peak before intercalation, the G0 peak indicates undoped graphene, while G1 and G2 correspond to higher carrier densities. To determine these carrier densities quantitatively, we varied the laser excitation energy. The peaks G1 and G2 exhibit maximum intensities at 1.96 eV and 2.07 eV excitation energies respectively, while the G0 peak intensity is relatively constant with excitation energy, as seen in figure 5.1b. The maximum in G peak intensity at a certain excitation energy signals that the local Fermi energy is half the excitation energy (C. F. Chen et al., 2011). Assuming that $FeCl_3$ is an acceptor molecule, we therefore determine that the Fermi energy corresponding to G0 is at the local Dirac point, while those for G1 and G2 are 0.98 eV and 1.03 eV below the local Dirac point, respectively, as illustrated in figure 5.1c. As the graphene layers are essentially decoupled, the number of free carriers in each region can be approximated *via* the relation $n \approx \frac{1}{\pi}(E_F/v_F\hbar)^2$ taken from table 1. We determine the carrier densities to be ~0 cm^{-2}, 7.1×10^{13} cm^{-2} and 7.8×10^{13} cm^{-2} for G0, G1, and G2 resonances respectively.

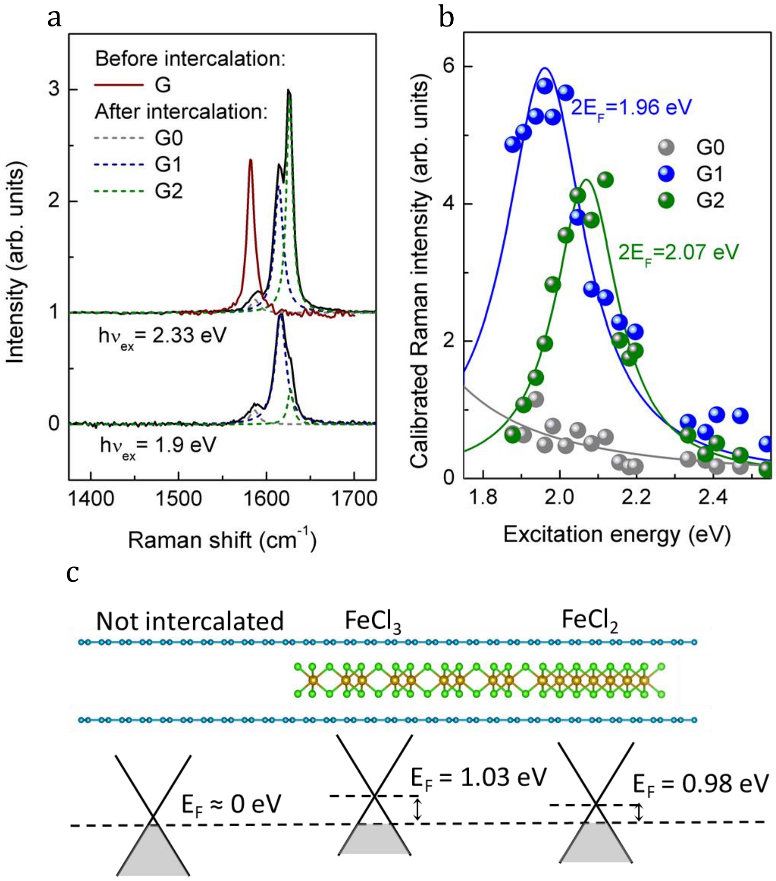

Figure 5.1: (a) Raman spectra for intercalated BLG- $FeCl_3$ in the region of G peak at 1.9 eV (bottom) and 2.33 eV (top) excitation energies (black). In addition, the G peak of pristine BLG before intercalation shown in the top graph in red. Dotted lines are Lorentzian fits of the G0, G1, and G2 peaks (b) Raman intensity of the G peaks as function of excitation energy. Peak maximum is achieved when laser energy matches twice the Fermi energy (c) A cartoon depiction of BLG intercalated with both $FeCl_3$ and $FeCl_2$ above a diagram of the respective relative Fermi energies.

5.2 Discussion of Spectroscopy Results

Combining the Raman spectroscopy results with the STEM data, we draw several conclusions about the atomic origin of the different free carrier densities. In the literature, the appearance of two blue-shifted G peaks is attributed to staging or surface adsorption of $FeCl_3$ (N. Kim, Kim, Jung, Brus, & Kim, 2011; W. Zhao et al., 2011). However, staging does not occur in BLG. In our STEM images, there is only a single monolayer of $FeCl_3$ between the layers of graphene and no adsorbed $FeCl_3$ on its surface. The presence of both the G1 and G2 peaks therefore indicates the presence of two different types of intercalants that locally induce different doping levels. We hypothesize that the coexistence of $FeCl_3$ and $FeCl_2$, as portrayed in figure 5.1c, is responsible for the two positions of the universal Fermi energy relative to the local Dirac points. This hypothesis is supported by DFT calculations that exhibit two different positions for the Fermi level below the Dirac point, 0.42 eV for $FeCl_2$ and 0.66 eV for $FeCl_3$. The smaller theoretical values of the Fermi energy relative to the local Dirac point compared to the experimental values is likely due to the underestimation of the Fermi velocity within the local density approximation (L. Yang, Deslippe, Park, Cohen, & Louie, 2009).

Overall, our DFT and Raman spectroscopy data suggest the association of the peaks G0, G1, and G2 with unintercalated regions, regions intercalated with $FeCl_2$, and regions intercalated with $FeCl_3$ respectively. Our STEM data are consistent with this assignment. The presence of the G0 peak is corroborated by the observation of unintercalated regions in STEM images, and the presence of the G1 and G2 peaks are corroborated by the observation of both intercalated $FeCl_3$ and $FeCl_2$ in the STEM images. The presence of $FeCl_3$ and $FeCl_2$ is also confirmed by measurements of oxidation state for the iron atoms *via* EELS as described in chapter 4.

5.3 Charge Distribution in Intercalant Systems

The appearance of free carriers (doping) in graphene layers adjacent to another material is typically interpreted as charge transfer. We used the present DFT-calculated charge densities in the intercalated BLG to test this interpretation. We find that, while the Fermi energy de*via*tes from the Dirac point in $FeCl_3$-BLG, there is virtually no net charge transfer between the graphene and intercalant layers. Although the lowering of the Fermi level below the Dirac point suggests a net transfer of electrons from the graphene to the intercalant, the valence-state wavefunctions in the $FeCl_3$ extend into the graphene layers thereby maintaining overall charge neutrality. In other words, the proximity of graphene to $FeCl_3$ causes a redistribution of electrons in the *energy space* to produce free carriers (doping), seemingly corresponding to charge transfer, but the distribution of electrons in physical space remains relatively unchanged.

5.3.1 Analysis of Charge Distribution in $FeCl_3$ Intercalants

Using DFT, the calculated density of states for $FeCl_3$-intercalated BLG is shown in figure 5.2a. It exhibits a Fermi energy of 0.66 eV below the Dirac point of the graphene layers, indicating a hole carrier density of 3.2×10^{13} cm^{-2}. This appearance of free carriers in graphene is usually assumed to be a result of charge transfer to or from graphene, in this case from the graphene to the intercalant. Such a conclusion, based solely on the shift of the Fermi level relative to the Dirac point, does not take into consideration what happens to the projected density of states (DOS) throughout the valence bands, and this conclusion must be corroborated by a demonstration that physical charge actually shifts in space from the graphene to the intercalant layer.

Assigning charge as belonging to individual atoms by examining the charge in spheres of chosen radii or some other polyhedrons centered around individual atoms, as in Mulliken

(Mulliken, 1955), Hirschfeld (Hirshfeld, 1977), or Bader (Bader, 1990) charges, entail diverse assumptions and are subject to ambiguities (Manz & Limas, 2016). For the issue at hand here, however, there is a particularly robust way to examine the question of charge transfer (Luo et al., 2007). We examine the DFT- calculated charge distribution around carbon atoms in pristine, freestanding, monolayer graphene and around several nonequivalent carbon atoms in the graphene layers of a $FeCl_3$-intercalated BLG structure. Using the nucleus of each carbon as the origin, we integrate the DFT-calculated electron density in concentric spheres of increasing radius (R) and plot the integrated charge as a function of R in figure 5.2b. The charge distribution around carbon atoms is indistinguishable in each case despite the presence of free holes, demonstrating that the electron density in graphene remains essentially undisturbed (*i.e.* the graphene sheets remain charge neutral). This conclusion is corroborated by similar plots for Fe atoms in freestanding $FeCl_3$ and $FeCl_3$-intercalated BLG in figure 5.2c. Once more the charge around Fe atoms remains undisturbed, demonstrating that the $FeCl_3$ layer does not actually hold any excess charge. The explanation of these results is that the wave functions of electrons nominally belonging to intercalant atoms extend over the graphene monolayers, restoring the overall charge neutrality of all carbon atoms. In other words, the manifestation of holes constitutes a redistribution of electrons in energy space, but not in physical space.

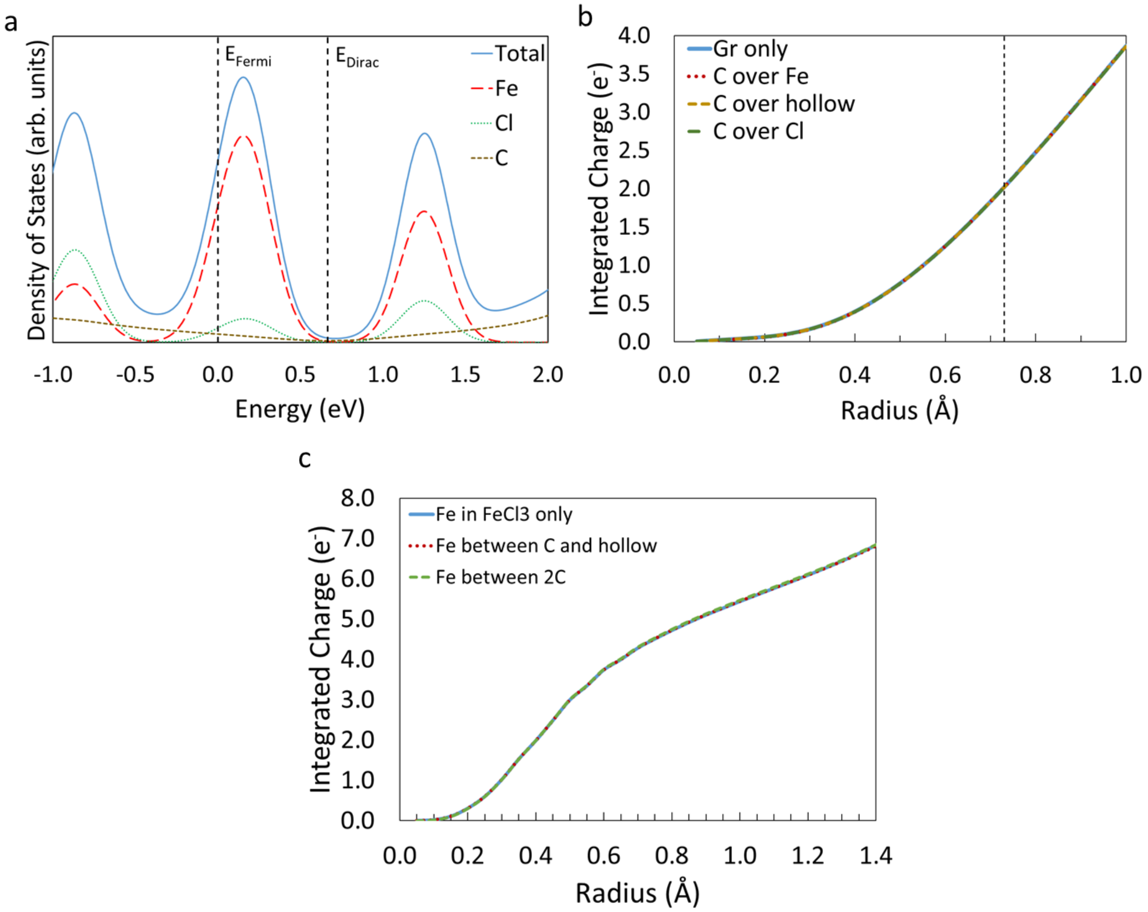

Figure 5.2: (a) Total density of states and site-projected density of states for each atomic species in the $FeCl_3$-intercalated bilayer graphene system. Black dashed lines represent the relative Fermi energy and Dirac-point energies, respectively. (b) Integrated charge within a sphere of radius R centered about a single carbon atom as a function of R in pure graphene and various positions in the $FeCl_3$-intercalated bilayer graphene system. The dashed line represents the carbon-carbon distance in graphene. (c) Integrated charge enclosed by spheres of radius R centered on a single iron atom as a function of R in free monolayer $FeCl_3$ and for various positions in the $FeCl_3$-intercalated bilayer graphene system.

5.3.2 Analysis of Charge Distribution in Lithium Intercalants

The absence of net physical-charge transfer accompanying the appearance of free carriers (doping) in graphene is also reinforced by a more simple example, namely Li adatoms on a freestanding graphene monolayer, which are known to induce the appearance of free electrons above the Dirac point (n-type doping in figure 5.3a for a coverage of 8.04×10^{13} Li/cm^2). Figure

5.3b shows the projected DOS in a low density of adsorbed Li atom, revealing that we have an empty Li 2s state above the Fermi level. This observation would commonly be interpreted as a net charge transfer, corresponding to the electrons above the Dirac point in graphene (figure 5.3a) and Li^+ ions on the surface. However, if the Li nucleus is used as the origin and charge is integrated in spheres of increasing radius (R) around it, we obtain a distribution that looks identical to the physical charge around a Li atom in Li metal, *i.e.* we do not have a Li^+ ion but neutral Li. These charge distributions are calculated in the same way and displayed figure 5.3c. Similar results are obtained for a high Li density. Note that the rise that occurs in Li adatom charge above ~1 Å from the center of the Li atom, as displayed in figure 5.3c, simply reflects the fact that the electrons from neighboring C atoms are also being counted at this distance. These results are fully consistent with contour plots of the charge around Li atoms adsorbed on graphene (Khantha, Cordero, Molina, Alonso, & Girifalco, 2004), though those authors interpreted their results in terms of charge transfer to the region between the Li adatom and graphene C atoms.

Further corroboration of the above analysis is provided by the long “tail” in the DOS in figure 5.3b, which is the result of carbon wavefunctions in the valence-band region extending over the Li atoms and restoring their neutrality. The number of states in that tail is in fact equal to the number of electrons in the sphere used to carry out the projected DOS calculations. In other words, although the Li 2s level lies above the Fermi energy and is empty, tails of carbon orbitals enter the Li space and make it neutral. This extension of the carbon orbitals can also be seen in figure 5.3d, which displays two-dimensional cutouts of the electron densities in the graphene valence bands that clearly show a finite electron density around the Li atoms and distortion of the carbon orbitals. This observation indicates that, although electrons from the Li

2s state are effectively transferred to the graphene layer, the electrons from the carbon p_z states extend to the Li atoms to maintain charge neutrality. These results are consistent with earlier findings that all atoms in so-called ionic crystals are effectively neutral, independent of the oxidation state (Luo et al., 2007). The conclusion is that when adatoms or other materials are in proximity to graphene, electrons in graphene are redistributed in energy space, resulting in free carriers either above or below the Dirac point (n-type or p-type doping). However, the electrons are not redistributed in physical space, resulting in no *net* charge transfer.

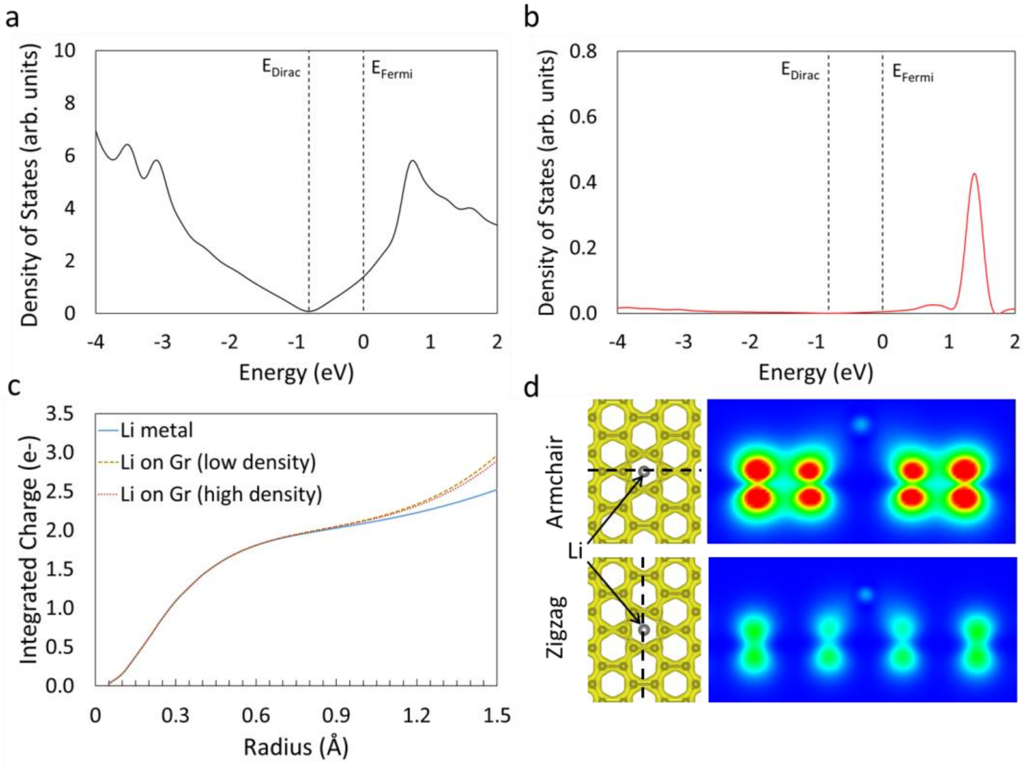

Figure 5.3: Density of states projected onto (a) the carbon atoms of the graphene layer and (b) Li atoms for 8.04×10^{13} Li/cm^2 concentration of Li adsorbed on graphene. (c) Comparison of the integrated charge on spheres of radius R centered on a Li atom in Li metal and the Li adsorbed on graphene in two different concentrations, as functions of R. (d) Two-dimensional cuts through the spatial partial charge density from the bottom of the valence band to the Fermi energy along (top) the armchair direction, cutting along carbon-carbon bonds, and (bottom) the zigzag direction, cutting between carbon-carbon bonds. Both directions show the presence of electron charge around the lithium site and distortions in the adjacent carbon p_z orbitals.

CHAPTER 6

Conclusions and Future Work

6.1 Possible Future Work

Direct continuation of this work would include optimizing the polymer electrolyte for *in situ* STEM devices to examine the atomic structure of electrochemically intercalated polyatomic ions. Additionally, protocols for CVT intercalation of $FeCl_3$ should be developed to determine the precise reaction conditions that produce the different atomic structure in $FeCl_3$-intercalated BLG, and protocols for CVT intercalation of other intercalant molecules should be developed to examine other possible monolayer materials that can be grown within BLG.

6.1.1 Continuation of Work on *In Situ* STEM Experiments

As mentioned in chapter 4, successful *in situ* STEM experiments will likely require doing tests on the electrolyte to ensure that the devices function properly. The polymer electrolyte for these devices needs to be mechanically robust to prevent migration of the polymers when a bias is applied. A crosslinked copolymer is used in which the mechanical stability is attributed to the covalent bonds between polymer units, but inducing too many crosslinked bonds also decreases the ion mobility in the electrolyte and prevents intercalation (Nair et al., 2012). Ionic conductivity and electrophoresis measurements should be implemented for polymer electrolytes with different ultraviolet (UV) doses to ensure sufficient ion mobility and allow intercalation without migration of the polymer. Additionally, the polymer electrolyte can degrade from high temperature exposure, and this degradation poses a problem for STEM devices, which require baking to remove residual moisture and hydrocarbons before entering the microscope. Thermal stability tests on the electrolyte using methods such as thermogravimetric analysis should be done to guarantee the devices function properly after the required baking protocol.

The intercalants used for electrochemical intercalation in this work were lithium and TSFI. Lithium intercalated in BLG exhibits a close-packed structure that achieves lithium densities greater than that of bulk GICs (Kühne et al., 2018), but to this date, we are unable to obtain similar data for TFSI intercalants. The data collected from such an experiment would be pivotal to the development of dual-graphite/FLG batteries (Read et al., 2014; Rothermel et al., 2014). Other intercalants should also be tested to develop a more complete model of the atomic structures in intercalation compounds. Similar experiments performed with other alkali metal intercalants would demonstrate whether other alkali metals exhibit the same close-packed structure as lithium. Such results could further elucidate why lithium has different intercalation behavior than sodium and potassium (Y. Liu, Merinov, & Goddard, 2016; Yabuuchi et al., 2014; J. Zhao, Zou, Zhu, Xu, & Wang, 2016). Furthermore, STEM experiments with intercalants such as $TFSI^-$, PF_6^-, and ClO_4^- would allow us to precisely determine the orientation, conformation, and intermolecular ordering of electrochemically intercalated polyatomic ions for development of novel battery chemistries (Beltrop et al., 2017; Fan, Qi, & Wang, 2017; Read et al., 2014; Rothermel et al., 2014). The results from such an experiment could also be combined with DFT calculations and used to test hypotheses about the stability of these intercalation products (Tasaki, 2014).

6.1.2 Continuation of Work on CVT Intercalation

Intercalating FLG and BLG with other intercalants *via* CVT intercalation is another avenue for continuing this work. We demonstrated that novel monolayer materials (*i.e.* $FeCl_3$, $FeCl_2$, and FeOCl) can be grown inside BLG and are stable to air and solvent exposure unlike freestanding forms of these materials (Bonacum et al., 2019). This discovery suggests other 2D materials that are not air-stable may also be grown in BLG with CVT intercalation to produce air-stable materials with properties like that of the freestanding counterparts. Some promising candidates for this work are CrI_3, which has the same crystal structure as $FeCl_3$, and $MnSe_2$, which has the same crystal structure as $FeCl_2$. Both of these materials have gained attention in recent years for the emergence of 2D ferromagnetism (Gibertini et al., 2019; Gong et al., 2017; Gong & Zhang, 2019; B. Huang et al., 2018; Jiang et al., 2018; Wan et al., 2016). These materials may also induce magnetism in the surrounding graphene layers *via* interlayer antiferromagnetic coupling (Bointon et al., 2015; N. Kim et al., 2011). After growing these materials with CVT intercalation, the magnetic properties can be measured with magnetic optical Kerr effect and magnetoresistance measurements to compare with results from the freestanding materials.

6.1.3 Optimization of $FeCl_3$ Intercalation

Lastly, further growth optimization and testing ought to be done with $FeCl_3$-BLG. Our results show that the composition of the intercalant layer in $FeCl_3$-BLG varies with reaction conditions. Variations in temperature result in incomplete intercalation; the presence of any reducing agents converts the $FeCl_3$ into $FeCl_2$, and exposure to energetic electrons produces FeOCl (Bonacum et al., 2019). These observations are important to consider when developing this material for applications such as battery electrodes, photodetectors, transparent conductors, and visible-spectrum plasmonic devices (De Sanctis et al., 2017; Khrapach et al., 2012; Qi et al., 2015; Shirodkar et al., 2018). These applications require highly uniform composition and resistance to degradation from chemical and lithographic processes during device fabrication. A standardized protocol is needed for synthesis and fabrication processes used to create devices with this material. Possible methods for developing these standardized protocols include doing precise measurements of the conditions during synthesis (*e.g.* reaction vessel volume, reactant concentration, temperature, and composition of trace elements inside the reaction vessel) and characterizing the material before and after fabrication techniques (*e.g.* lithography and chemical/reactive-ion etching). For this work, we formed our reaction vessels from glass tubing with a butane torch, evacuated the reaction vessels with a two-stage rotary vane pump, and controlled the temperature with a tube furnace. The shape/volume of the reaction vessel was imprecise due to the difficulty in molding the reaction vessel with the butane torch, and we were only able to achieve 0.5 mTorr inside the reaction vessel with the two-stage rotary vane pump. We were also only able to measure the temperature at one location inside the tube furnace that we used for the reaction. To remedy these issues, we suggest using a commercial ampoule vacuum sealing machine connected to a turbo pump, which would produce reaction vessels with a consistent shape and volume that can be sealed under ultrahigh vacuum. Finally, the temperature should be regulated with sections of heat tape and multiple thermal couples connected to proportional-integral-derivative (PID) controllers for precise control of the temperature throughout the reaction vessel.

6.2 Concluding Remarks on Current Work

In conclusion, this work demonstrates that intercalation of molecules in BLG or FLG can lead to the formation of diverse complex structures. We observed the formation of crystalline $FeCl_3$ monolayers with a honeycomb structure like that of bulk $FeCl_3$, atomically sharp boundaries between intercalated and unintercalated regions, the presence of defects, and a variety of possible orientations for the $FeCl_3$ relative to graphene layers. This information is useful for the study of interesting phenomena in graphene such as Klein tunneling of Dirac-like fermions, which requires atomically sharp doping boundaries, and the study of effects on the electronic band structure of graphene due to superlattice formation between the $FeCl_3$ and graphene honeycomb lattices (Katsnelson, Novoselov, & Geim, 2006; Young & Kim, 2009). The observation of iron interstitial defects also has possible applications in information storage due to modification of the local magnetic field by the defects. We provide evidence for coexistence of both $FeCl_3$ and $FeCl_2$ in BLG under ambient conditions, which was not observed previously and could provide a new perspective for interpreting the stability of $FeCl_3$-intercalated FLG. Specifically, our results suggest that previously reported changes in the Raman spectra of FLG-$FeCl_3$ might be due to the formation of $FeCl_2$ rather than deintercalation of $FeCl_3$ (Wehenkel et al., 2015; W. Zhao et al., 2011). Additionally, we demonstrate the conversion of monolayer $FeCl_3$ into FeOCl *via* an electron-beam-induced reaction inside BLG, revealing intercalated BLG to be a useful vessel for creating novel 2D materials.

APPENDIX A

Sample Fabrication

A.1 Mechanical Exfoliation

We use the common “Scotch tape method” for mechanical exfoliation (Novoselov, 2004). The materials we use are kish graphite from Graphene Supermarket and Scotch® brand Magic™ tape. First, we make a master tape by putting a few pieces of the kish graphite on a piece of tape, folding the tape over the graphite pieces, and then peeling the tape apart to separate and expose clean surfaces of the graphite. Another piece of tape is then placed on top of the master tape and peeled off to remove thin layers of graphite. That tape is placed on the substrate taking care to avoid any air bubbles between the tape and substrate. We then exfoliate the graphite by gently rubbing the top of the tape with a plastic card for a few minutes. Only about a pound of force is required. Too much force will break the graphite apart and result in small fragments of bulk graphite on the substrate. Finally, we peel off the tape as slowly as possible by hand, allowing the graphene layer in contact with the substrate to separate from the bulk graphite on the tape. This method works well for hard substrates such as thermally grown silicon oxide, which is the substate used for devices described in chapter 2, referring to figures 2.1-2.3.

A.2 Viscoelastic Transfer Method

For the STEM compatible device, we use a viscoelastic transfer method to position the FLG on a silicon membrane with micron precision (Castellanos-Gomez et al., 2014). This is a dry transfer method, which does not require any wet chemical cleaning post-transfer. Instead, the viscoelastic transfer relies on the deformation properties of the viscoelastic stamp. Viscoelastic solids react to deformation differently depending on the rate of deformation, and the FLG is attached or released from the stamp by using different deformation rates. We opt for this transfer method to avoid additional contamination of the samples with polymers that are used in other transfer methods.

The viscoelastic material we use is polydimethylsiloxane (PDMS), which is made by following the steps below:

1. Mix 30 g of elastomer base (Sylgard^{TM} 184 silicone elastomer base) with 1.5 g of curing agent (Sylgard^{TM} 184 silicone elastomer curing agent).
2. Evenly pour the mixture into two 10 cm by 10 cm square dishes.
3. Place the dishes in a vacuum chamber for 10 minutes to degas the mixture.
4. Bake in an oven at 60 ^{o}C for 3 hours for curing

To prepare the transfer stamp, we cut out a 2 cm square of the PDMS from the dish and place on a clean glass slide, being careful to avoid any air bubbles between the PDMS and the glass. The graphite is then mechanically exfoliated onto to the PMDS using the "Scotch tape method" as described in the previous section. However, when exfoliating on a viscoelastic substrate, the tape must be pulled from the substrate quickly because viscoelastic PDMS acts differently at different time scales. The PDMS behaves as an elastic solid for peel velocities on the order of 10 cm/s, and it behaves more as a viscous liquid for peel velocities on the order of 1 mm/s (Meitl et al., 2006).

Once an appropriate FLG flake is located on the transfer stamp, the sample is attached to the sample stage with double-sided Kapton tape, and the glass slide holding the stamp is mounted to a transfer stage like the example shown in figure A.1a. We then use the x-axis and yaxis controls to locate and position the FLG flake over the location we want place to it. The z-axis control is used to lower the stamp towards the sample. It is often necessary to refocus the objective and reposition the flake as it is being lowered. When the stamp is in contact with the sample, it is heated to 100 ^{o}C for at least 10 minutes using resistive heating elements inside the sample stage that are connected to a PID controller. The heat helps improve adhesion between the FLG flake and the substrate by aggregating contaminates in the interface.

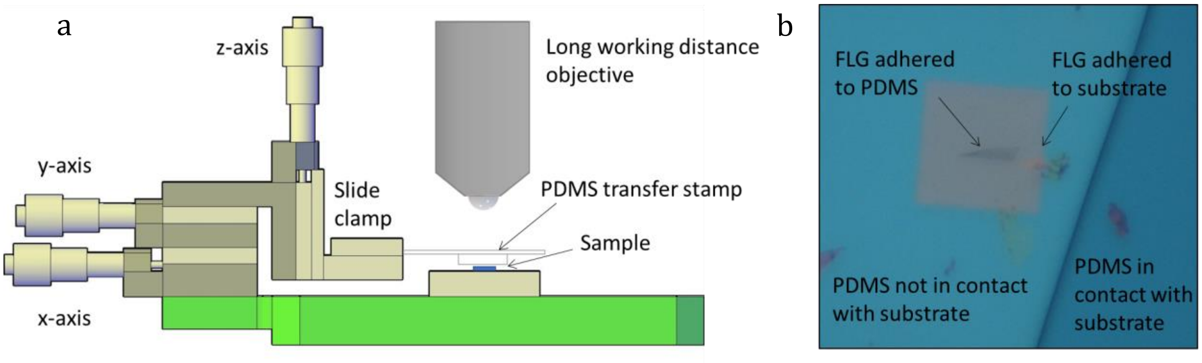

Figure A.1: (a) Schematic of the transfer stage used for deterministic transfers of FLG (b) Optical image of the sample during the transfer process.

Finally, we slowly remove the stamp using the z-axis control. Doing this step slowly is essential for a successful transfer because the PDMS stamp must behave as a viscous liquid to release the FLG, and this release only occurs at sufficiently slow peel velocities. For this work, we use a minimum peel velocity of 1 μm/s. The peel rate can be estimated while looking through the objective by looking at the speed of the interface between the PDMS that is in contact and not in contact with the substate. An example of this interface is displayed in figure A.1b. Success of the transfer can also be seen through the objective by looking at the color and contrast of the FLG. Figure A.1b shows a FLG flake transferred to a silicon nitride membrane. The left side of the FLG appears as a gray color because the transfer was initiated with a peel velocity that was too fast, and the FLG did not release onto the membrane. The right side of the FLG released onto the membrane once the peel velocity was slowed down sufficiently, and this side of the FLG is nearly transparent with low contrast to the membrane.

A.3 Electron Beam Lithography

We use electron beam lithography (EBL) to define the electrodes on our FLG devices as illustrated in figure A.2.

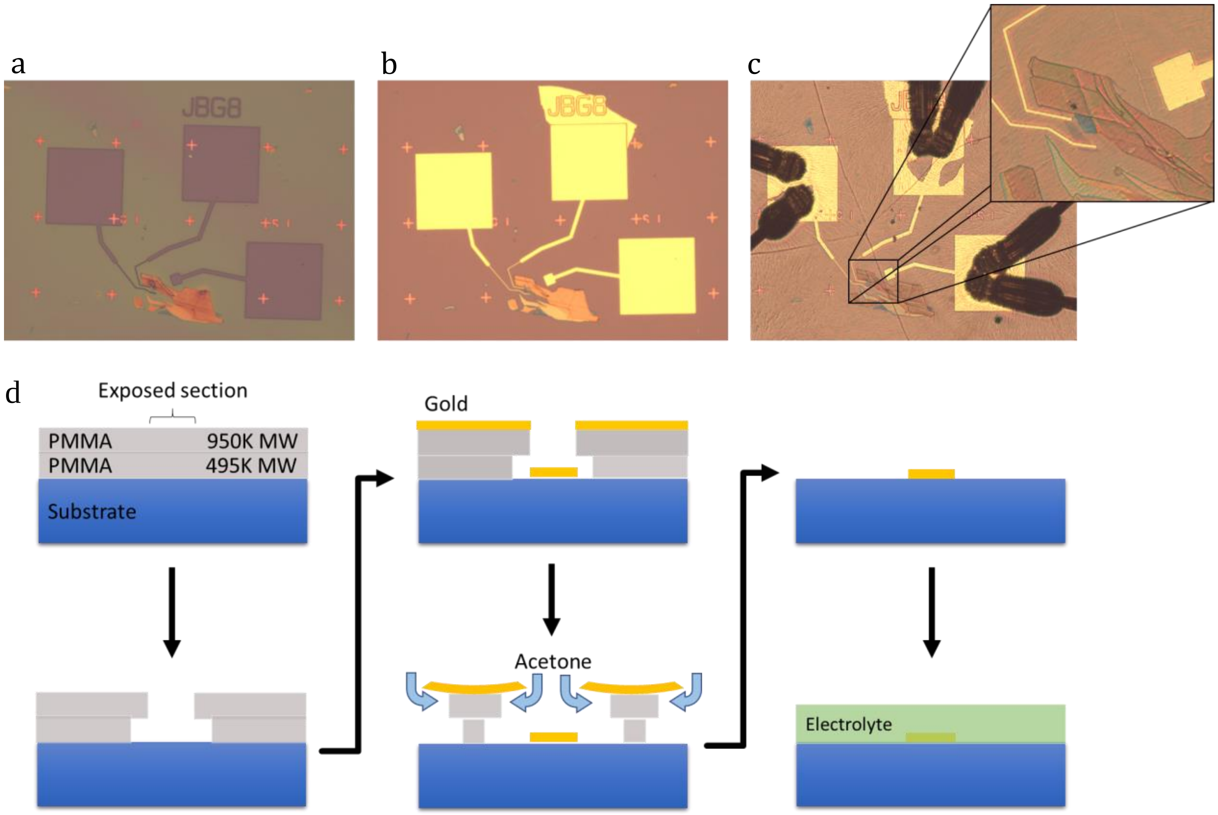

Figure A.2: Optical image of FLG device after (a) electron-beam patterning and development (b) metal deposition and liftoff (c) wire bonding and drop-casting the electrolyte with an inset showing the device at higher magnification. (d) A diagram showing the lithography steps. The steps performed prior to each optical image are positioned below the images.

The first step of the EBL process is spin coating the resist, the material in which the electrode pattern will be written with the electron beam. We use two layers of polymethyl methacrylate (PMMA) for the resist. The top layer is 950K molecular weight (MW), and the bottom layer is 495K MW. For spin coating, we use 6% PMMA solutions by weight in anisole. Both layers are spun at 4000 RPM for 45 seconds followed by baking at 180 ^{o}C for 2 minutes to evaporate the solvent.

The electrode patterns are written with a Raith eLine scanning electron microscope. We use a 20.00 kV accelerating voltage, 10 mm working distance, and 30-micron aperture in the microscope when writing micron-sized features on uniform substrates. For devices on silicon nitride membranes like those shown in figure 2.5, we use a 10.00 kV accelerating voltage to even out the effective dose difference between features over the membrane and over the silicon substrate. Much less electron backscattering and secondary emission occurs in the freestanding silicon nitride membrane at higher accelerating voltages, resulting in a lower effective dose received by the resist in those locations. Using 10.00 kV as the accelerating voltage remedies this under-dosing problem on the membrane at the cost of lower writing resolution, but the decreased resolution is not a problem for features larger than a micron.

After writing the pattern, the resist is developed with a one-to-three ratio of methyl isobutyl ketone and isopropyl alcohol (1:3 MIBK:IPA) for 1 minute followed by 5 seconds in IPA to stop development. The 495K MW PMMA develops faster than the 950K MW PMMA resulting in the undercut profile of the resist depicted in figure A.2d. This undercut profile provides more space for solvent to contact the resist when we need to remove it later in the lithography process. We then blow dry the sample with nitrogen gas to remove any excess IPA and check the pattern in an optical microscope. An example of an EBL pattern after development is displayed in figure A.2a.

The metal for the electrodes is deposited using electron-beam physical vapor deposition in an Angstrom Amod deposition system. We first deposit 2 nm of either titanium or chromium as an adhesion layer between the electrode and substrate. We then deposit 70 nm of gold or platinum for the bulk of the electrode. After the metal for the electrode is deposited, we place the sample in acetone at 90 ^{o}C and agitate with a pipet to dissolve the resist and lift off the excess metal as depicted in figure A.2d. An optical image of a device after liftoff is displayed in figure A.2b.

A.4 Electrolyte Preparation

We use two types of polymer electrolytes in this work. The first electrolyte we used is polyethylene oxide lithium bis(trifluoromethanesulfonyl)imide (PEO LiTFSI), which uses a transfer solvent for deposition. The PEO LiTFSI is dissolved in the transfer solvent (acetonitrile), and then the transfer solvent is evaporated leaving the solid PEO LiTSFI on the device. The protocol used is as follows:

1. Heat 20 mL of acetonitrile at 90 ^{o}C for 2 minutes with a stir bar at 500 RPM.
2. Slowly add 0.3 g of PEO and 0.05 g of LiTFSI salt in a low humidity, preferably inert, environment.
3. Centrifuge the solution at 6000 RPM for 15 minutes to separate the excess polymer and precipitates.
4. Drop cast on the sample and bake at 90 ^{o}C for 30 minutes to evaporate off the acetonitrile.

The other electrolyte we used is poly(ethylene glycol) methyl ether methacrylate – bisphenol A ethoxylate dimethacrylate copolymer lithium bis(trifluoromethanesulfonyl)imide (PEGMA-BEMA LiTFSI). This electrolyte does not require a transfer solvent because the polymer used is a copolymer that requires UV radiation. The electrolyte is a viscous liquid before curing and becomes a solid after curing when the PEGMA and BEMA become crosslinked forming the copolymer matrix. The protocol for this electrolyte is as follows:

1. Weigh out 150 mg of LiTFSI salt in an inert environment and transfer to an airtight vile to limit absorption of water in the salt.
2. Measure out 1.1 mL of 1700M.W. BEMA using a 1mL syringe with 0.01 mL marks & transfer to the vile
3. Measure out 0.4 mL of 475M.W. PEGMA using a 1 mL syringe with 0.01mL marks & transfer to the vile
4. Measure out 0.045 mL of 2-hydroxy-2methylpropiophenone (photo-initiator) using a 1 mL syringe with 0.01 mL marks & transfer to the vile
5. Stir for ~1 min until visually homogenous using the photo-initiator syringe
6. Close vile and wrap in Al foil to prevent premature curing
7. Deposit on the sample using a needle-tipped microfluidic syringe under UV blocked lighting
8. Place the sample in a UV blocking sample holder for transport to the UV source
9. Cure the electrolyte using a 5800 mJ/cm^2 dose from a mercury fluorescence lamp

A.5 Few-layer and Bilayer Graphene Fabrication for $FeCl_3$ Intercalation

The FLG was mechanically exfoliated from kish graphite onto PDMS using Scotch tape. The support grid for the FLG was prepared by milling 2 μm apertures in 50 nm silicon nitride membranes (PELCO Silicon Nitride Support Films) with a Helios Nanolab G3 CX dual beam focus ion beam – scanning electron microscope, and the FLG was then transferred to the silicon nitride membrane over the apertures using a viscoelastic stamp transfer method (Castellanos-Gomez et al., 2014). The BLG samples were purchased commercially (Graphene on PELCO Holey Silicon Nitride). Graphene in these samples was grown by chemical vapor deposition.

A.6 Chemical Vapor Transport Method for $FeCl_3$

The vapor transport method of intercalation involves vacuum-sealing the FLG and $FeCl_3$ powder inside an ampoule and then annealing, which causes the $FeCl_3$ to evaporate and spontaneously intercalate into the FLG. The ampule is prepared by sealing one end of a ¼ inch diameter borosilicate tube with a butane torch and then baking overnight at 150 ^oC to remove moisture. Then 0.02 g of $FeCl_3$ were transferred to the ampule, and the ampule was evacuated to 5 mTorr with an Edwards 5 two-stage rotary-vane vacuum pump. The ampule is attached to the vacuum setup using a quick-connect coupler. To ensure that the $FeCl_3$ is anhydrous, the ampule is heated to 120 ^oC for 30 min during evacuation and purged three times with nitrogen gas. The sample was then inserted into the ampoule, and the evacuation procedure was repeated. Once the ampule pressure gets down to 0.5 mTorr, a butane torch was used to seal the ampoule approximately 10 cm from the opposite end of the $FeCl_3$ powder. The ampule was then annealed is a Lindenburg Blue M 1-inch tube furnace to initiate the intercalation reaction. For the reaction process, the tube furnace was heated to 340 ^oC (measured at the center) with a ramp rate of 1

^{o}C/s and PID setting of 20-120-30. The reaction takes place over six hours with the ampoule 5 cm from the center, which results in a temperature difference of ~15 ^{o}C between the FLG and $FeCl_3$ powder. Finally, the tube furnace was cooled at a rate of 1 ^{o}C/s, and the intercalated sample was then removed by scoring and breaking open the ampule.

APPENDIX B

Sample Characterization

B.1 Initial Characterization of FLG-$FeCl_3$ Samples

Figure A.3a shows the reaction vessel and an optical image of the FLG sample as described in chapter 3. The $FeCl_3$-intercalated FLG samples were characterized by atomic force microscopy (AFM), Raman spectroscopy, and EELS. Examples of these data are given in figure A.3, which shows data for the FLG with nearly aligned $FeCl_3$ discussed in chapter 3, and figure A.4 shows data for the intercalated BLG. The shape of the 2D peak around 2700 cm^{-1} in figure A.3c shows that the FLG graphene is more than three layers thick, while the AFM height profile in figure A.3b confirms a thickness of four to six layers (Malard et al., 2009; Shearer, Slattery, Stapleton, Shapter, & Gibson, 2016). When the FLG is intercalated by $FeCl_3$, the graphene layers undergo hole doping, and each graphene layer can be doped by either one $FeCl_3$ layer between the graphene layers or by two $FeCl_3$ layers on each side. This discrete doping is manifested in the Raman spectra as the appearance of two blue-shifted G peaks, because the G peak blue shifts linearly with doping due to the Kohn anomaly at the K point in the graphene phonon band structure (Froehlicher & Berciaud, 2015; Lazzeri & Mauri, 2006; W. Zhao et al., 2011). For the FLG samples in this work, the Raman spectrum after intercalation indicates partial intercalation, as evidenced by blue shifting and splitting of the G peak, and the EELS of the FLG after intercalation verifies the presence of carbon, iron, and chlorine atoms.

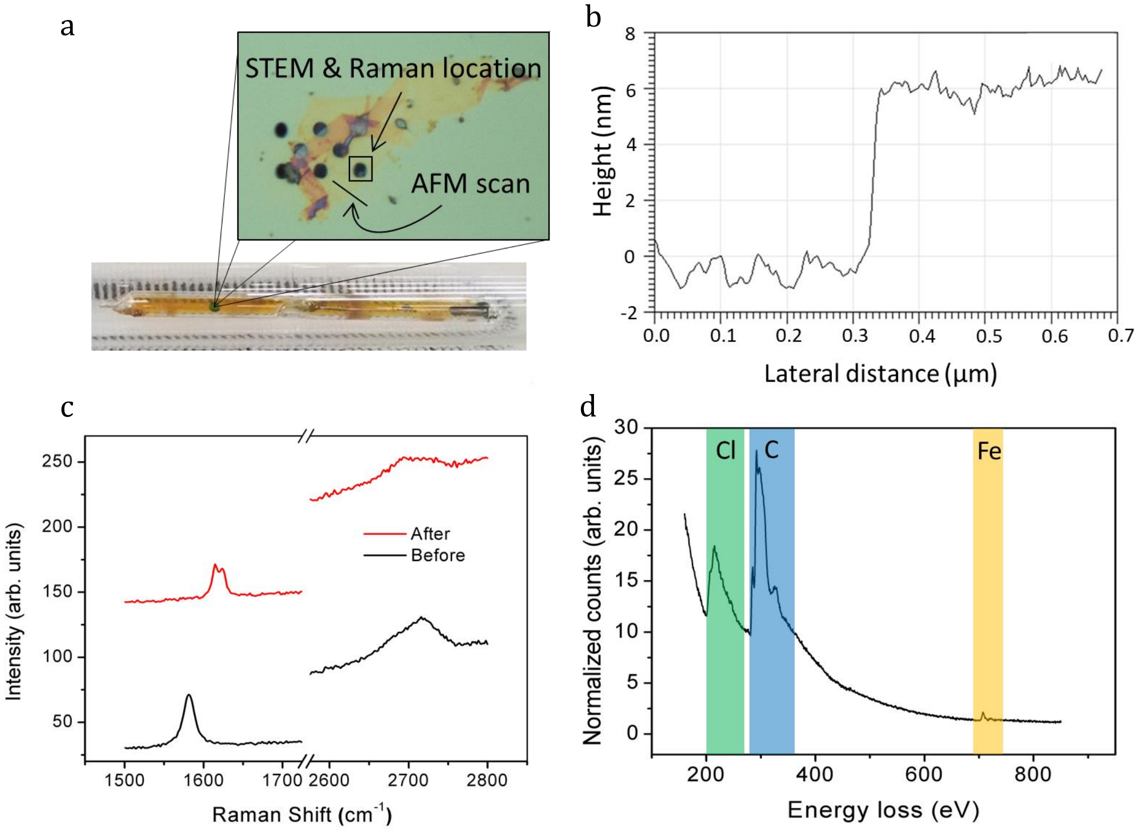

Figure B.1: (a) Image of $FeCl_3$-intercalated FLG sample on a milled silicon nitride membrane, showing the location of STEM, Raman spectroscopy, and AFM measurements (b) AFM height profile before intercalation (c) Raman spectra before and after intercalation (d) Electron energy loss spectrum (EELS) with labels for the chlorine, carbon, and iron signatures.

B.2 Initial Characterization of BLG-$FeCl_3$ Samples

For the BLG samples, the G peak may also split after intercalation, exemplified in figure A.4b, but the lower wave number peak corresponds to undoped graphene. This splitting is due to incomplete formation of the $FeCl_3$ layer inside the BLG, which is why intercalation boundaries can be seen in the STEM data. The EELS spectrum also verifies the presence of carbon, iron, and chlorine.

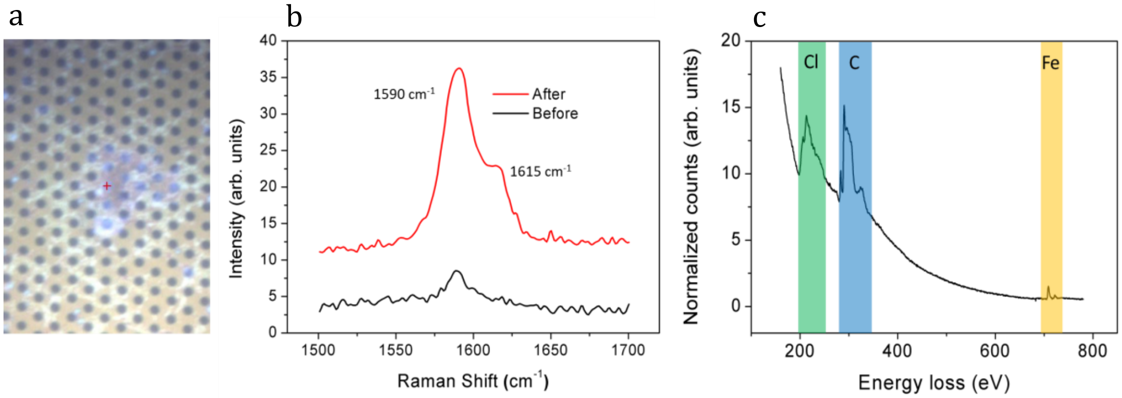

Figure B.2: (a) Image of intercalated BLG on holey silicon nitride (b) Raman spectra before and after intercalation (b) EELS with labels for the chlorine, carbon, and iron signatures

APPENDIX C

Measurement Parameters

C.1 Scanning Transmission Electron Microscopy

All ADF images were acquired using an aberration-corrected Nion UltraSTEM 100^{TM} operated at 60 kV accelerating voltage to prevent damage to the graphene layers (Krivanek et al., 2008). We used a semi-angle convergence of 30 mrad and ADF-detection semi-angle range of 86-200 mrad for the intercalated FLG samples, and we used a detection semi-angle of 54-200 mrad for the intercalated BLG samples. Additionally, the length scales in our data were compared with a reference sample to ensure accuracy of the measured lengths for this work.

C.2 Resonance-Raman Spectroscopy

The resonance-Raman spectra were obtained at the same spot on the intercalated sample. A tunable laser system with a dye laser (Radiant dye: 550-675 nm) and an Ar-Kr laser (Coherent Innova 70c: 450-530 nm) were used to excite the sample. The laser power was limited to 500 µW to avoid heat-induced effects (100x microscope objective). The light was dispersed by a T64000 Horba Jobin Yvon spectrometer equipped with 900 grooves per mm grating and a silicon charge-coupled device in single detection mode and backscattering configuration. Elastically scattered light was rejected by a long pass filter. The Raman shift was calibrated on a benzonitrile reference molecule and the Raman intensity of pristine bilayer graphene to account for the wavelength dependent spectrometer sensitivity.

APPENDIX D

Data Analysis

D.1 Moiré Lattice Constant Derivation

The moiré lattice is formed by interference between two slightly mismatched lattices. One example of this concept is the formation of beats between two oscillating functions:

$$\begin{aligned} e^{i\vec{k}_1\cdot\vec{r}} + e^{i\vec{k}_2\cdot\vec{r}} &= e^{i\frac{(\vec{k}_1+\vec{k}_2)}{2}\cdot\vec{r}}\, e^{i\frac{(\vec{k}_1-\vec{k}_2)}{2}\cdot\vec{r}} + e^{i\frac{(\vec{k}_1+\vec{k}_2)}{2}\cdot\vec{r}}\, e^{-i\frac{(\vec{k}_1-\vec{k}_2)}{2}\cdot\vec{r}} \\ &= 2\left[\cos\left(\frac{\vec{k}_1+\vec{k}_2}{2}\cdot\vec{r}\right)\cos\left(\frac{\vec{k}_1-\vec{k}_2}{2}\cdot\vec{r}\right) + i\sin\left(\frac{\vec{k}_1+\vec{k}_2}{2}\cdot\vec{r}\right)\cos\left(\frac{\vec{k}_1-\vec{k}_2}{2}\cdot\vec{r}\right)\right] \end{aligned} \quad (6)$$

Plotting the real part in one dimension gives:

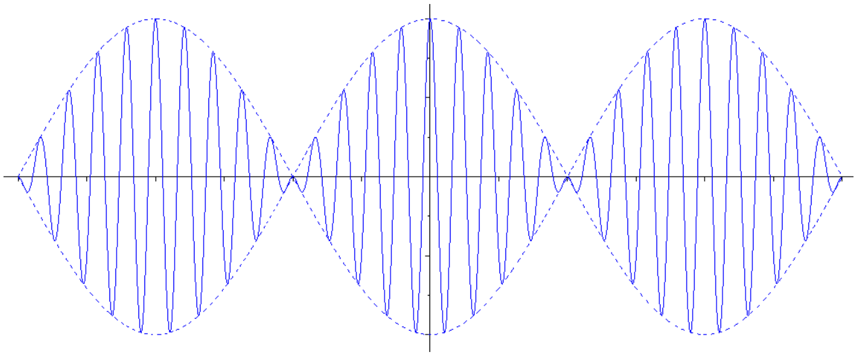

The dotted line represents the envelope function, which displays the moiré pattern, and this envelope function has a wavevector of $\overrightarrow{k_1} - \overrightarrow{k_2}$. Additionally, this derivation can be applied to any periodic function using a Fourier expansion. Thus, the reciprocal lattice vector for the moiré lattice is the difference between the reciprocal lattice vectors of the lattices that interfere to form the moiré lattice.

$$\vec{b}_{moiré} = \vec{b}_\alpha - \vec{b}_\beta \quad (7)$$

The vector $\vec{b}_{moiré}$ is the reciprocal lattice vector for the moiré lattice, and the vectors $\overrightarrow{b_\alpha}$ and $\overrightarrow{b_\beta}$ are the reciprocal lattice vectors for the α and β lattices that form the moiré lattice.

For this work, the α and β lattices are identical with a lattice parameter a=0.61nm and rotated by an angle (θ) relative to one another. Using a coordinate system with $\overrightarrow{b_\alpha}$ in the x direction:

$$\left|\vec{b}_\alpha\right| = \left|\vec{b}_\beta\right| = \frac{2\pi}{a} \tag{8}$$

$$\vec{b}_\alpha = \frac{2\pi}{a}\begin{pmatrix} 1 \\ 0 \end{pmatrix} \tag{9}$$

$$\vec{b}_\beta = \begin{pmatrix} \cos\theta & -\sin\theta \\ \sin\theta & \cos\theta \end{pmatrix}\vec{b}_\alpha = \frac{2\pi}{a}\begin{pmatrix} \cos\theta \\ \sin\theta \end{pmatrix} \tag{10}$$

Combining equations 7-10 yields:

$$\left|\vec{b}_{moiré}\right| = \frac{2\pi}{a}\sqrt{2(1-\cos\theta)} = \frac{2\pi}{a_{moiré}} \tag{11}$$

Solving for $a_{moiré}$ gives equation 5 in chapter 3:

$$a_{moiré} = \frac{a}{\sqrt{2(1-\cos\theta)}} \tag{12}$$

D. 2 Second Derivative Spectroscopy Analysis

Since multiple effects contribute to the EELS background – namely the zero-loss peak and core-loss edges – fitting the white-line peaks in the raw data is difficult. However, fitting these peaks is critical to calculating the iron L_3/L_2 white-line intensity ratio, which in turn determines the oxidation state of the iron atoms. Analyzing the second derivative of the data allows us to determine the ratio without having to fit and subtract the background (Botton, Appel, Horsewell, & Stobbs, 1995). For Gaussian and Lorentzian peak shapes, the intensity ratio is equal to the ratio of the second derivative minimum multiplied by the ratio of the peak variances, which can be determined from the zeros of the second derivative. The derivation for this is shown below.

Figure A.5 shows spectral lines and their second derivatives for both Lorentzian and Gaussian line shapes, as well as the EELS data from our sample that exhibit $FeCl_2$ intercalated in BLG. For both Lorentzian and Gaussian line shapes, the L_3/L_2 white-line intensity ratio is given by:

$$\frac{y(x_0)_{L_3}}{y(x_0)_{L_2}} = \frac{y''(x_0)_{L_3}}{y''(x_0)_{L_2}} \frac{\alpha_{L_3}{}^2}{\alpha_{L_2}{}^2} \tag{13}$$

where $y(x_0)$ is the maximum value at the center of the spectral line, $y''(x_0)$ is value of the second derivative at x_0, and α is the zero of the second derivative measured with respect to x_0 (*i.e.* $\alpha = x(y''=0)-x_0$).

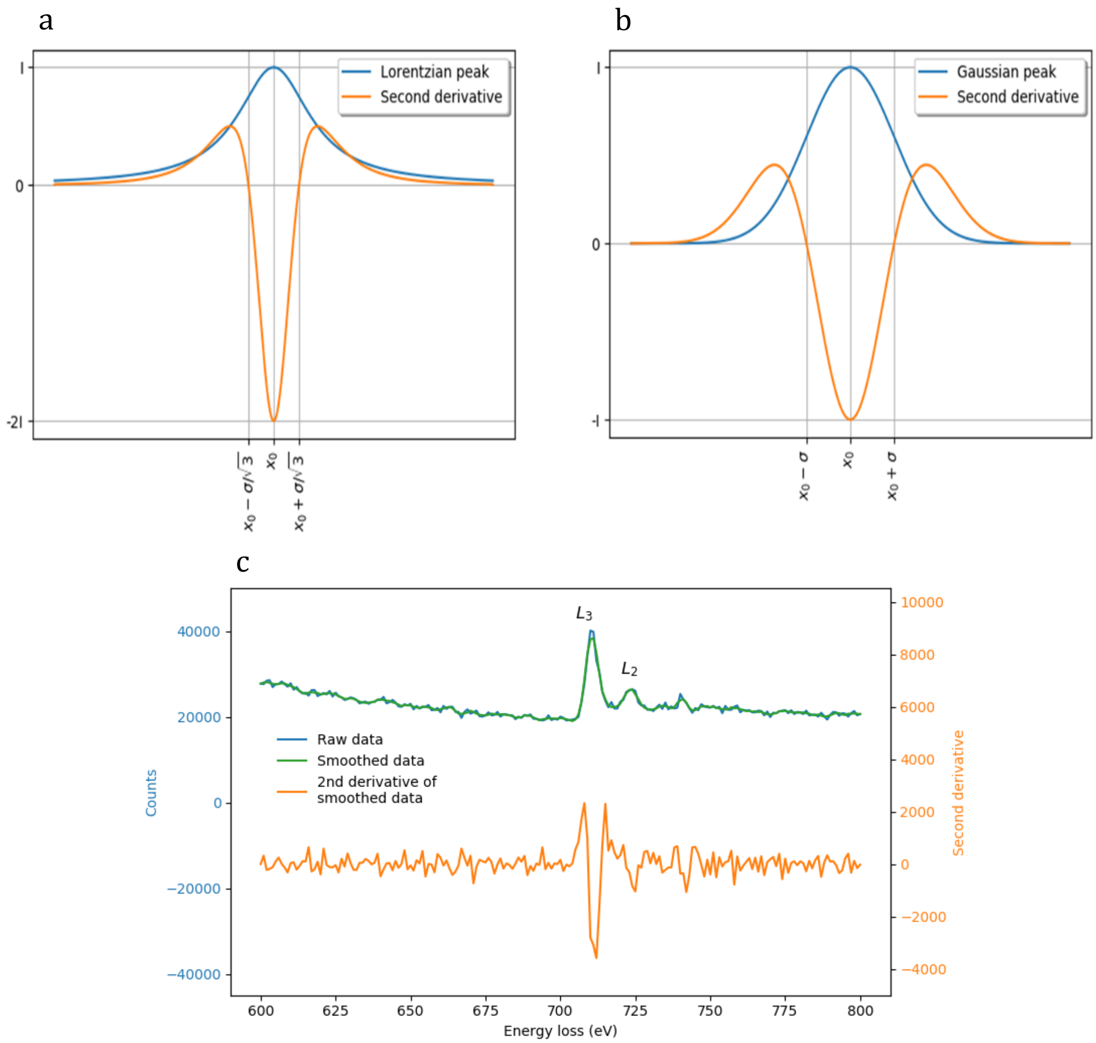

Figure D.1: A plot of a (a) Lorentzian and (b) Gaussian spectral line shape and the second derivatives. The vertical and horizontal lines in the plots show the extrema and zeros. (c) EELS of $FeCl_2$ and the second derivative of the data.

D.2.1 Derivation for Lorentzian Line Shape

The Lorentzian line shape is given by the function:

$$L(x) = \frac{L_{\max}}{1+\left(\frac{x-x_0}{\sigma}\right)^2} \tag{14}$$

where L$_{\max}$ is the maximum of the spectral line, x_0 is the location of the spectral line, and σ is the half width at half maximum. The second derivative evaluated at x_0 is

$$L''(x_0) = -2\frac{L_{\max}}{\sigma^2} \tag{15}$$

Using equation 14 and 15 to write a ratio of L_3 and L_2 intensities gives

$$\frac{L_{\max,L_3}}{L_{\max,L_2}} = \frac{L(x_0)_{L_3}}{L(x_0)_{L_2}} = \frac{L''(x_0)_{L_3}}{L''(x_0)_{L_2}}\frac{\sigma_{L_3}{}^2}{\sigma_{L_2}{}^2} \tag{16}$$

The half width at half maximum can also be written in terms of the zeros of the second derivative.

$$\alpha_{Lorentzian} = \pm\frac{\sigma}{\sqrt{3}} \tag{17}$$

Solving for σ and inserting in equation 16 gives equation 13 for a Lorentzian line shape.

D.2.2. Derivation for Gaussian Line Shape

The Gaussian line shape is given by the function:

$$G(x) = G_{\max} e^{-\frac{(x-x_0)^2}{2\sigma^2}} \tag{18}$$

where G$_{\max}$ is the maximum of the spectral line, x_0 is the location of the spectral line, and σ is the standard de*via*tion. The second derivative evaluated at x_0 is

$$G''(x_0) = -\frac{L_{\max}}{\sigma^2} \tag{19}$$

Using equation 18 and 19 to write a ratio of L_3 and L_2 intensities gives

$$\frac{G_{\max,L_3}}{G_{\max,L_2}} = \frac{G(x_0)_{L_3}}{G(x_0)_{L_2}} = \frac{G''(x_0)_{L_3}}{G''(x_0)_{L_2}}\frac{\sigma_{L_3}{}^2}{\sigma_{L_2}{}^2} \tag{20}$$

The standard de*via*tion can also be written in terms of the zeros of the second derivative.

$$\alpha_{Lorentzian} = \pm\sigma \tag{21}$$

Solving for σ and inserting in equation 20 gives equation 13 for a Gaussian.

Figure A.5c displays the EELS iron edge of the sample shown in figure 4.1d in chapter 4. The experimental L_3/L_2 white-line intensity ratio for this section of our sample is 4±1, supporting the hypothesis that this structure is indeed $FeCl_2$.

REFERENCES

Al-Jishi, R. (1983). Model for superconductivity in graphite intercalation compounds. *Physical Review B*, **28**, 112.

Aronson, S. (1963). Bromine exchange in graphite-bromine lamellar compounds. *Journal of Inorganic and Nuclear Chemistry*, **25**, 907–918.

Asher, R. C. (1959). A lamellar compound of sodium and graphite. *Journal of Inorganic and Nuclear Chemistry*, **10**, 238–249.

Axdal, S. H. A., & Chung, D. D. L. (1987). Kinetics and thermodynamics of intercalation of bromine in graphite-I. Experimental. *Carbon*, **25**, 191–210.

Azhagurajan, M., Kajita, T., Itoh, T., Kim, Y., & Itaya, K. (2016). *In Situ Visualization of Lithium Ion Intercalation into MoS 2 Single Crystals using Di ff erential Optical Microscopy with Atomic Layer Resolution*. https://doi.org/10.1021/jacs.5b11849

Bader, R. F. W. (1990). *Atoms in Molecules: A Quantum Theory*. New York: Oxford University Press.

Bao, W., Wan, J., Han, X., Cai, X., Zhu, H., Kim, D., Ma, D., Xu, Y., Munday, J. N., Drew, H. D., Fuhrer, M. S., & Hu, L. (2014). Approaching the limits of transparency and conductivity in graphitic materials through lithium intercalation. *Nature Communications*, **5**, 1–9.

Bardeen, J., Cooper, L. N., & Schrieffer, J. R. (1957). Microscopic Theory of Superconductivity. *Physical Review*, **106**, 162–164.

Beltrop, K., Beuker, S., Heckmann, A., Winter, M., & Placke, T. (2017). Alternative electrochemical energy storage: Potassium-based dual-graphite batteries. *Energy and Environmental Science*, **10**, 2090–2094.

Bezares, F. J., Sanctis, A. De, Saavedra, J. R. M., Woessner, A., Alonso-González, P., Amenabar, I., Chen, J., Bointon, T. H., Dai, S., Fogler, M. M., Basov, D. N., Hillenbrand, R., Craciun, M. F., García De Abajo, F. J., Russo, S., & Koppens, F. H. L. (2017). Intrinsic Plasmon-Phonon Interactions in Highly Doped Graphene: A Near-Field Imaging Study. *Nano Letters*, **17**, 5908–5913.

Boersma, M. A. M. (1974). Catalytic Properties of Alkali Metal-Graphite Intercalation Compounds. *Catalysis Reviews*, **10**, 243–280.

Bointon, T. H., Khrapach, I., Yakimova, R., Shytov, A. V., Craciun, M. F., & Russo, S. (2015). Approaching magnetic ordering in graphene materials by FeCl3 intercalation. *Nano Letters*, **14**, 1751–1755.

Bonacum, J. P., O'Hara, A., Bao, D.-L., Ovchinnikov, O. S., Zhang, Y.-F., Gordeev, G., Arora, S., Reich, S., Idrobo, J.-C., Haglund, R. F., Pantelides, S. T., & Bolotin, K. I. (2019). Atomic-resolution visualization and doping effects of complex structures in intercalated bilayer graphene. *Physical Review Materials*, **3**, 064004.

Botton, G. A., Appel, C. C., Horsewell, A., & Stobbs, W. M. (1995). Quantification of the EELS near-edge structures to study Mn doping in oxides. *Journal of Microscopy*, **180**, 211–216.

Castellanos-Gomez, A., Buscema, M., Molenaar, R., Singh, V., Janssen, L., Van Der Zant, H. S. J., & Steele, G. A. (2014). Deterministic transfer of two-dimensional materials by all-dry viscoelastic stamping. *2D Materials*, **1**, 1.

Castro Neto, A. H., Guinea, F., Peres, N. M. R., Novoselov, K. S., & Geim, A. K. (2009). The electronic properties of graphene. *Reviews of Modern Physics*, **81**, 109–162.

Chen, C. F., Park, C. H., Boudouris, B. W., Horng, J., Geng, B., Girit, C., Zettl, A., Crommie, M. F., Segalman, R. A., Louie, S. G., & Wang, F. (2011). Controlling inelastic light scattering quantum pathways in graphene. *Nature*, **471**, 617–620.

Chen, F., Qing, Q., Xia, J., Li, J., & Tao, N. (2009). Electrochemical Gate-Controlled Charge Transport in Graphene in Ionic Liquid and Aqueous Solution. *Journal of the American Chemical Society*, **131**, 9908–9909.

Chen, J.-H., Jang, C., Xiao, S., Ishigami, M., & Fuhrer, M. S. (2008). Intrinsic and extrinsic performance limits of graphene devices on SiO2. *Nature Nanotechnology*, **3**, 206–209.

Cohn, A. P., Muralidharan, N., Carter, R., Share, K., & Pint, C. L. (2016). Durable potassium ion battery electrodes from high-rate cointercalation into graphitic carbons. *Journal of Materials Chemistry A: Materials for Energy and Sustainability*, **4**, 14954–14959.

Cohn, A. P., Share, K., Carter, R., Oakes, L., & Pint, C. L. (2016). Ultrafast Solvent-Assisted Sodium Ion Intercalation into Highly Crystalline Few-Layered Graphene. *Nano Letters*, **16**, 543–548.

Cowley, J. M., & Ibers, J. A. (1956). The structures of some ferric chloride–graphite compounds. *Acta Crystallographica*, **9**, 421–431.

Csányi, G., Littlewood, P. B., Nevidomskyy, A. H., Pickard, C. J., & Simons, B. D. (2005). The role of the interlayer state in the electronic structure of superconducting graphite intercalated compounds. *Nature Physics*, **1**, 42–45.

Das, A., Pisana, S., Chakraborty, B., Piscanec, S., Saha, S. K., Waghmare, U. V, Novoselov, K. S., Krishnamurthy, H. R., Geim, A. K., Ferrari, A. C., & Sood, A. K. (2008). *Monitoring dopants by Raman scattering in an electrochemically top-gated graphene transistor*. **3**, 1–6.

De Sanctis, A., Jones, G. F., Wehenkel, D. J., Bezares, F., Koppens, F. H. L., Craciun, M. F., & Russo, S. (2017). Extraordinary linear dynamic range in laser-defined functionalized graphene photodetectors. *Science Advances*, **3**. https://doi.org/10.1126/sciadv.1602617

Dimiev, A. M., Ceriotti, G., Behabtu, N., Zakhidov, D., Pasquali, M., Saito, R., & Tour, J. M. (2013). Direct real-time monitoring of stage transitions in graphite intercalation compounds. *ACS Nano*, **7**, 2773–2780.

Dresselhaus, M. S., & Dresselhaus, G. (2002). Intercalation compounds of graphite. *Advances in Physics*, **511**, 1–186.

Ebert, L. B. (1984). Electrochemistry of Intercalation Compounds of Graphite. *Proceedings - The Electrochemical Society*, **84–5**, 595–607.

Fan, H., Qi, L., & Wang, H. (2017). Hexafluorophosphate anion intercalation into graphite electrode from methyl propionate. *Solid State Ionics*, **300**, 169–174.

Fan, H., Qi, L., Yoshio, M., & Wang, H. (2017). Hexafluorophosphate intercalation into graphite electrode from ethylene carbonate/ethylmethyl carbonate. *Solid State Ionics*, **304**, 107–112.

Froehlicher, G., & Berciaud, S. (2015). Raman spectroscopy of electrochemically gated graphene transistors: Geometrical capacitance, electron-phonon, electron-electron, and electron-defect scattering. *Physical Review B*, **91**, 205413.

Gibertini, M., Koperski, M., Morpurgo, A. F., & Novoselov, K. S. (2019). Magnetic 2D materials and heterostructures. *Nature Nanotechnology*, **14**, 408–419.

Gong, C., Li, L., Li, Z., Ji, H., Stern, A., Xia, Y., Cao, T., Bao, W., Wang, C., Wang, Y., Qiu, Z. Q., Cava, R. J., Louie, S. G., Xia, J., & Zhang, X. (2017). Discovery of intrinsic ferromagnetism in two-dimensional van der Waals crystals. *Nature*, **546**, 265–269.

Gong, C., & Zhang, X. (2019). Two-dimensional magnetic crystals and emergent heterostructure devices. *Science*, **363**. https://doi.org/10.1126/science.aav4450

Gusynin, V. P., Sharapov, S. G., & Carbotte, J. P. (2006). Unusual Microwave Response of Dirac Quasiparticles in Graphene. *Physical Review Letters*, **96**, 256802.

Hennig, G. R. (2007). *Interstitial Compounds of Graphite* (F. A. Cotton, ed.). https://doi.org/10.1002/9780470166024.ch2

Hirshfeld, F. L. (1977). Bonded-atom fragments for describing molecular charge densities. *Theor. Chim. Acta*, **44**, 129–138.

Hooley, J. G. (1973). Isotherms of metal chloride vapors on graphite. *Carbon*, **11**, 225–236.

Hooley, J. G., & Bartlett, M. (1967). The intercalation isotherm of ferric chloride vapor on graphite from 300 to 350°C. *Carbon*, **5**, 417–422.

Huang, B., Clark, G., Klein, D. R., MacNeill, D., Navarro-Moratalla, E., Seyler, K. L., Wilson, N., McGuire, M. A., Cobden, D. H., Xiao, D., Yao, W., Jarillo-Herrero, P., & Xu, X. (2018). Electrical control of 2D magnetism in bilayer CrI3. *Nature Nanotechnology*, **13**, 544–548.

Huang, X., Leng, T., Chang, K. H., Chen, J. C., Novoselov, K. S., & Hu, Z. (2016). Graphene radio frequency and microwave passive components for low cost wearable electronics. *2D Materials*, **3**, 025021.

Hui, J., Burgess, M., Zhang, J., & Rodríguez-López, J. (2016). Layer Number Dependence of Li+Intercalation on Few-Layer Graphene and Electrochemical Imaging of Its Solid-Electrolyte Interphase Evolution. *ACS Nano*, **10**, 4248–4257.

Hwang, S. R., Li, W.-H., Lee, K. C., Lynn, J. W., & Wu, C.-G. (2000). Spiral magnetic structure of Fe in Van der Waals gapped FeOCl and polyaniline-intercalated FeOCl. *Physical Review B*, **62**, 14157–14163.

Jiang, S., Shan, J., & Mak, K. F. (2018). Electric-field switching of two-dimensional van der Waals magnets. *Nature Materials*, **17**, 406–410.

Joucken, F., Henrard, L., & Lagoute, J. (2019). Electronic properties of chemically doped graphene. *Physical Review Materials*, **3**, 110301.

Kanetani, K., Sugawara, K., Sato, T., Shimizu, R., Iwaya, K., Hitosugi, T., & Takahashi, T. (2012). Ca intercalated bilayer graphene as a thinnest limit of superconducting C6Ca. *Proceedings of the National Academy of Sciences*, **109**, 19610–19613.

Katsnelson, M. I., Novoselov, K. S., & Geim, A. K. (2006). Chiral tunnelling and the Klein paradox in graphene. *Nature Physics*, **2**, 620–625.

Khantha, M., Cordero, N. A., Molina, L. M., Alonso, J. A., & Girifalco, L. A. (2004). Interaction of lithium with graphene: An ab initio study. *Physical Review B*, **70**, 125422.

Khrapach, I., Withers, F., Bointon, T. H., Polyushkin, D. K., Barnes, W. L., Russo, S., & Craciun, M. F. (2012). Novel highly conductive and transparent graphene-based conductors. *Advanced Materials*, **24**, 2844–2849.

Kim, K. S., Zhao, Y., Jang, H., Lee, S. Y., Kim, J. M., Kim, K. S., Ahn, J.-H., Kim, P., Choi, J.-Y., & Hong, B. H. (2009). Large-scale pattern growth of graphene films for stretchable transparent electrodes. *Nature*, **457**, 706–710.

Kim, N., Kim, K. S., Jung, N., Brus, L., & Kim, P. (2011). Synthesis and electrical characterization of magnetic bilayer graphene intercalate. *Nano Letters*, **11**, 860–865.

Kim, S. J., Park, S. J., Kim, H. Y., Jang, G. S., Park, D. J., Park, J.-Y., Lee, S., & Ahn, Y. H. (2016). Characterization of chemical doping of graphene by in-situ Raman spectroscopy. *Applied Physics Letters*, **108**, 203111.

Krivanek, O. L., Corbin, G. J., Dellby, N., Elston, B. F., Keyse, R. J., Murfitt, M. F., Own, C. S., Szilagyi, Z. S., & Woodruff, J. W. (2008). An electron microscope for the aberration-corrected era. *Ultramicroscopy*, **108**, 179–195.

Kühne, M., Börrnert, F., Fecher, S., Ghorbani-asl, M., Biskupek, J., Samuelis, D., Krasheninnikov, A. V, Kaiser, U., & Smet, J. H. (2018). Reversible superdense ordering of lithium between two graphene sheets. *Nature*, **564**, 234–239.

Kühne, M., Paolucci, F., Popovic, J., Ostrovsky, P. M., Maier, J., & Smet, J. H. (2017). Ultrafast lithium diffusion in bilayer graphene. *Nature Nanotechnology*, **12**, 895–900.

Lalancette, J.-M., Rollin, G., & Dumas, P. (1972). Metals Intercalated in Graphite. I. Reduction and Oxidation. *Canadian Journal of Chemistry*, **50**, 3058–3062.

Lazzeri, M., & Mauri, F. (2006). Nonadiabatic Kohn anomaly in a doped graphene monolayer. *Physical Review Letters*, **97**, 266407.

Lee, J., Zhou, W., Idrobo, J. C., Pennycook, S. J., & Pantelides, S. T. (2011). Vacancy-driven anisotropic defect distribution in the battery-cathode material LiFePO 4. *Physical Review Letters*, **107**, 085507.

Li, Y., & Yue, Q. (2013). First-principles study of electronic and magnetic properties of FeCl3-based graphite intercalation compounds. *Physica B: Condensed Matter*, **425**, 72–77.

Lin, P.-C., Wu, J.-Y., & Liu, W.-R. (2018). Green and facile synthesis of few-layer graphene *via* liquid exfoliation process for Lithium-ion batteries. *Scientific Reports*, **8**, 9766.

Lind, M. D. (1970). Refinement of the crystal structure of iron oxychloride. *Acta Cryst. B*, **26**, 1058–1062.

Liu, H., Liu, Y., & Zhu, D. (2011). Chemical doping of graphene. *J. Mater. Chem.*, **21**, 3335–3345.

Liu, Y., Merinov, B. V., & Goddard, W. A. (2016). Origin of low sodium capacity in graphite and generally weak substrate binding of Na and Mg among alkali and alkaline earth metals. *Proceedings of the National Academy of Sciences of the United States of America*, **113**, 3735–3739.

Lu, X., & Zhao, C. (2013). Controlled electrochemical intercalation, exfoliation and in situ nitrogen doping of graphite in nitrate-based protic ionic liquids. *Physical Chemistry Chemical Physics*, **15**, 20005.

Luo, W., Franceschetti, A., Varela, M., Tao, J., Pennycook, S. J., & Pantelides, S. T. (2007). Orbital-Occupancy versus Charge Ordering and the Strength of Electron Correlations in Electron-Doped. *Physical Review Letters*, **99**, 036402.

Lv, R., Li, Q., Botello-Méndez, A. R., Hayashi, T., Wang, B., Berkdemir, A., Hao, Q., Eléas, A. L., Cruz-Silva, R., Gutiérrez, H. R., Kim, Y. A., Muramatsu, H., Zhu, J., Endo, M., Terrones, H., Charlier, J. C., Pan, M., & Terrones, M. (2012). Nitrogen-doped graphene: Beyond single substitution and enhanced molecular sensing. *Scientific Reports*, **2**, 586.

Malard, L. M., Pimenta, M. A., Dresselhaus, G., & Dresselhaus, M. S. (2009). Raman spectroscopy in graphene. *Physics Reports*, **473**, 51–87.

Manz, T. A., & Limas, N. G. (2016). Introducing DDEC6 atomic population analysis: part 1. Charge partitioning theory and methodology. *RSC Advances*, **6**, 47771–47801.

McGuire, M. A., Dixit, H., Cooper, V. R., & Sales, B. C. (2015). Coupling of Crystal Structure and Magnetism in the Layered, Ferromagnetic Insulator CrI 3. *Chemistry of Materials*, **27**, 612–620.

Meitl, M. A., Zhu, Z.-T., Kumar, V., Lee, K. J., Feng, X., Huang, Y. Y., Adesida, I., Nuzzo, R. G., & Rogers, J. A. (2006). Transfer printing by kinetic control of adhesion to an elastomeric stamp. *Nature Materials*, **5**, 33–38.

Mulliken, R. S. (1955). Electronic Population Analysis on LCAO-MO Molecular Wave Functions. *The Journal of Chemical Physics*, **23**, 1833–1840.

Nair, J. R., Chiappone, A., Destro, M., Jabbour, L., Meligrana, G., & Gerbaldi, C. (2012). UV-Induced Radical Photo-Polymerization: A Smart Tool for Preparing Polymer Electrolyte Membranes for Energy Storage Devices. *Membranes*, **2**, 687–704.

Nandkishore, R., Levitov, L. S., & Chubukov, A. V. (2012). Chiral superconductivity from repulsive interactions in doped graphene. *Nature Physics*, **8**, 158–163.

Nilsson, J., Neto, A. H. C., Guinea, F., & Peres, N. M. R. (2006). Electronic Properties of Graphene Multilayers. *Physical Review Letters*, **97**, 266801.

Nitta, N., Wu, F., Lee, J. T., & Yushin, G. (2015). Li-ion battery materials: Present and future. *Materials Today*, **18**, 252–264.

Nixon, D. E., & Parry, G. S. (1968). Formation and structure of the potassium graphites. *Journal of Physics D: Applied Physics*, **1**, 303.

Novikov, Y. N., & Vol'pin, M. E. (1971). Lamellar Compounds of Graphite with Alkali Metals. *Russian Chemical Reviews*, **40**, 733–746.

Novoselov, K. S. (2004). Electric Field Effect in Atomically Thin Carbon Films. *Science*, **306**, 666–669.

Ovchinnikov, O. S., O'Hara, A., Nicholl, R. J. T., Hachtel, J. A., Bolotin, K., Lupini, A., Jesse, S., Baddorf, A. P., Kalinin, S. V, Borisevich, A. Y., & Pantelides, S. T. (2018). Theory-assisted determination of nano-rippling and impurities in atomic resolution images of angle-mismatched bilayer graphene. *2D Materials*, **5**, 041008.

Palumbo, S., Silvestri, L., Ansaldo, A., Brescia, R., Bonaccorso, F., & Pellegrini, V. (2019). Silicon Few-Layer Graphene Nanocomposite as High-Capacity and High-Rate Anode in Lithium-Ion Batteries. *ACS Applied Energy Materials*, **2**, 1793–1802.

Pierantoni, L., Mencarelli, D., Bozzi, M., Moro, R., Moscato, S., Perregrini, L., Micciulla, F., Cataldo, A., & Bellucci, S. (2015). Broadband Microwave Attenuator Based on Few Layer Graphene Flakes. *IEEE Transactions on Microwave Theory and Techniques*, **63**, 2491–2497.

Podall, H., & Foster, W. E. (1958). Catalytic Graphite Inclusion Compounds. II. Potassium Graphite as an Alkylation Catalyst. *Journal of Organic Chemistry*, **23**, 401–403.

Qi, X., Qu, J., Zhang, H.-B., Yang, D., Yu, Y., Chi, C., & Yu, Z.-Z. (2015). FeCl3 intercalated few-layer graphene for high lithium-ion storage performance. *Journal of Materials Chemistry A*, **3**, 15498–15504.

Rakoczy, J., Klimkiewicz, R., & Morawski, A. W. (1996). Application of K-Bi-graphite intercalation compounds as stereoselective catalysts of cyclohexanol conversion. *Journal of Physics and Chemistry of Solids*, **57**, 805–808.

Read, J. A., Cresce, A. V., Ervin, M. H., & Xu, K. (2014). Dual-graphite chemistry enabled by a high voltage electrolyte. *Energy and Environmental Science*, **7**, 617–620.

Rothermel, S., Meister, P., Schmuelling, G., Fromm, O., Meyer, H. W., Nowak, S., Winter, M., & Placke, T. (2014). Dual-graphite cells based on the reversible intercalation of bis(trifluoromethanesulfonyl)imide anions from an ionic liquid electrolyte. *Energy and Environmental Science*, **7**, 3412–3423.

Rüdorff, W. (1959). Graphite Intercalation Compounds. *Advances in Inorganic Chemistry and Radiochemistry*, **1**, 223–266.

Rudorff, W., & Zeller, R. (1955). Uber Aluminiumchlorid-Graphit-Einlagerungsverbindungen. *Zeitschrift Fur Anorganische Und Allgemeine Chemie*, **279**, 182–193.

Salzano, F. J., & Aronson, S. (1965). Thermodynamic Properties of the Cesium—Graphite Lamellar Compounds. *The Journal of Chemical Physics*, **43**, 149–154.

Salzano, F. J., & Aronson, S. (1966). Thermodynamic properties of rubidium-graphite lamellar compounds. *The Journal of Chemical Physics*, **45**, 4551–4555.

Share, K., Cohn, A. P., Carter, R. E., & Pint, C. L. (2016). Mechanism of potassium ion intercalation staging in few layered graphene from in situ Raman spectroscopy. *Nanoscale*, **8**, 16435–16439.

Shearer, C. J., Slattery, A. D., Stapleton, A. J., Shapter, J. G., & Gibson, C. T. (2016). Accurate thickness measurement of graphene. *Nanotechnology*, **27**, 12.

Shimizu, A., & Kamimura, H. (1983). Theory of superconductivity in graphite intercalation compounds. *Synthetic Metals*, **5**, 301–313.

Shirodkar, S. N., Mattheakis, M., Cazeaux, P., Narang, P., Soljačić, M., & Kaxiras, E. (2018).

Quantum plasmons with optical-range frequencies in doped few-layer graphene. *Physical Review B*, **97**. https://doi.org/10.1103/PhysRevB.97.195435

Sole, C., Drewett, N. E., & Hardwick, L. J. (2014). Insitu Raman study of lithium-ion intercalation into microcrystalline graphite. *Faraday Discussions*, **172**, 223–237.

Somnath, S., Smith, C. R., Kalinin, S. V., Chi, M., Borisevich, A., Cross, N., Duscher, G., & Jesse, S. (2018). Feature extraction *via* similarity search: application to atom finding and denoising in electron and scanning probe microscopy imaging. *Advanced Structural and Chemical Imaging*, **4**, 3.

Tarascon, J. M., & Armand, M. (2001). Issues and challenges facing rechargeable lithium batteries. *Nature*, **414**, 359–367.

Tasaki, K. (2014). Density functional theory study on structural and energetic characteristics of graphite intercalation compounds. *Journal of Physical Chemistry C*, **118**, 1443–1450.

Wallace, P. R. (1947). The Band Theory of Graphite. *Physical Review*, **71**, 622–634.

Wan, J., Lacey, S. D., Dai, J., Bao, W., Fuhrer, M. S., & Hu, L. (2016). Tuning two-dimensional nanomaterials by intercalation: Materials, properties and applications. *Chemical Society Reviews*, **45**, 6742–6765.

Wehenkel, D. J., Bointon, T. H., Booth, T., Bøggild, P., Craciun, M. F., & Russo, S. (2015). Unforeseen high temperature and humidity stability of FeCl3 intercalated few layer graphene. *Scientific Reports*, **5**, 7609.

Wei, D., Liu, Y., Wang, Y., Zhang, H., Huang, L., & Yu, G. (2009). Synthesis of N-Doped Graphene by Chemical Vapor Deposition and Its Electrical Properties. *Nano Letters*, **9**, 1752–1758.

Weller, T. E., Ellerb, M., Saxena, S. S., Smith, R. P., & Skipper, N. T. (2005). Superconductivity in the intercalated graphite compounds C6Yb and C6Ca. *Nature Physics*, **1**, 39–41.

Wen, Y., He, K., Zhu, Y., Han, F., Xu, Y., Matsuda, I., Ishii, Y., Cumings, J., & Wang, C. (2014). Expanded graphite as superior anode for sodium-ion batteries. *Nature Communications*, **5**, 1–10.

Woltornist, S. J., Oyer, A. J., Carrillo, J.-M. Y., Dobrynin, A. V., & Adamson, D. H. (2013). Conductive Thin Films of Pristine Graphene by Solvent Interface Trapping. *ACS Nano*, **7**, 7062–7066.

Yabuuchi, N., Kubota, K., Dahbi, M., & Komaba, S. (2014). Research development on sodium-ion batteries. *Chem. Rev.*, **114**, 11636–11682.

Yang, L., Deslippe, J., Park, C.-H., Cohen, M. L., & Louie, S. G. (2009). Excitonic Effects on the

Optical Response of Graphene and Bilayer Graphene. *Physical Review Letters*, **103**, 186802.

Yang, Z. hong, & Wu, H. qing. (2001). Electrochemical intercalation of lithium into carbon nanotubes. *Solid State Ionics*, **143**, 173–180.

Yoshino, A. (2012). The birth of the lithium-ion battery. *Angewandte Chemie - International Edition*, **51**, 5798–5800.

Young, A. F., & Kim, P. (2009). Quantum interference and Klein tunnelling in graphene heterojunctions. *Nature Physics*, **5**, 222–226.

Zhang, L., Chen, L., Luo, H., Zhou, X., & Liu, Z. (2017). Large-Sized Few-Layer Graphene Enables an Ultrafast and Long-Life Aluminum-Ion Battery. *Advanced Energy Materials*, **7**, 1700034.

Zhao, J., Zou, X., Zhu, Y., Xu, Y., & Wang, C. (2016). Electrochemical Intercalation of Potassium into Graphite. *Advanced Functional Materials*, **26**, 8103–8110.

Zhao, W., Tan, P. H., Liu, J., & Ferrari, A. C. (2011). Intercalation of few-layer graphite flakes with FeCl3: Raman determination of Fermi level, layer by layer decoupling, and stability. *Journal of the American Chemical Society*, **133**, 5941–5946.